


Effects of elastoviscoplastic properties of mucus on airway closure in healthy and pathological conditions

O. Erken ^{*}, B. Fazla , and M. Muradoglu [†]

Department of Mechanical Engineering, Koc University, Rumeli Feneri Yolu, 80910 Sariyer, Istanbul, Turkey

D. Izbassarov 

*Finnish Meteorological Institute, Erik Palmelin aukio 1, 00560 Helsinki, Finland
and Department of Mechanical Engineering, Aalto University, FI-00076, Espoo, Finland*

F. Romand 

*University of Lille, CNRS, ONERA, Arts et Métiers Institute of Technology, Centrale Lille, UMR 9014, LMFL,
Laboratoire de Mécanique des Fluides de Lille, Kampé de Fériet, F-59000 Lille, France*

J. B. Grotberg

Department of Biomedical Engineering, University of Michigan, Ann Arbor, Michigan 48109, USA



(Received 28 September 2022; accepted 31 March 2023; published 19 May 2023)

Airway mucus is a complex material with both viscoelastic and viscoplastic properties that vary with healthy and pathological conditions of the lung. In this study, the effects of these conditions on airway closure are examined in a model problem, where an elastoviscoplastic (EVP) single liquid layer lines the inner wall of a rigid pipe and surrounds the air core. The EVP liquid layer is modelled using the Saramito-HB model. The parameters for the model are obtained for the mucus in healthy, asthma, chronic obstructive pulmonary disease (COPD), and cystic fibrosis (CF) conditions by fitting the rheological model to the experimental data. Then the liquid plug formation is studied by varying the Laplace number and undisturbed liquid film thickness. Airway closure is a surface-tension-driven phenomenon that occurs when the ratio of the pulmonary liquid layer thickness to the airway radius exceeds a certain threshold. In previous studies, it has been found that airway epithelial cells can be lethally or sublethally damaged due to the high peak of the wall stresses and stress gradients during the liquid plug formation. Here we demonstrate that these stresses are also related to the EVP features of the liquid layer. Yielded zones of the liquid layer are investigated for the different mucus conditions, and it is found that the liquid layer is in a chiefly unyielded state before the closure, which indicates that this phase is dominated by the elastic behavior and solvent viscosity. This is further confirmed by showing that the elastic coefficient is one of the most critical parameters determining whether the closure occurs. This parameter also largely affects the closure time. The wall stresses are also investigated for the pathological and healthy cases. Their peaks for COPD

^{*}Present address: School of Engineering, Institute for Infrastructure and Environment, The University of Edinburgh, United Kingdom.

[†]Corresponding author: mmuradoglu@ku.edu.tr

Published by the American Physical Society under the terms of the [Creative Commons Attribution 4.0 International](https://creativecommons.org/licenses/by/4.0/) license. Further distribution of this work must maintain attribution to the author(s) and the published article's title, journal citation, and DOI.

and CF are found to be the highest due to the viscoelastic extra stress contribution. Contrary to the Newtonian case, the wall stresses for COPD and CF do not smoothly relax after closure, as they rather remain effectively almost as high as the Newtonian peak. Moreover, the local normal wall stress gradients are smaller for the COPD and CF liquid layer due to their higher stiffness causing a smaller curvature at the capillary wave. The local tangential wall stress gradients are also shown to be smaller for these cases because of the slower accumulation of the liquid at the bulge.

DOI: [10.1103/PhysRevFluids.8.053102](https://doi.org/10.1103/PhysRevFluids.8.053102)

I. INTRODUCTION

The inner surface of airways is covered with a liquid film, called airway surface liquid (ASL). The diameter of the airways decreases gradually from the trachea to the alveolar sacs, and this can be characterized to leading order by the correlation $a_j = a_0 2^{(-j/3)}$ for the first 14 generations, where a_0 is the diameter of the trachea and a_j is the diameter of the airway at j th generation [1]. The lung can be divided into two parts, which are the conducting and the respiratory zones. The first 16 generations are the conducting zone that includes the trachea, the bronchi, the bronchioles and the terminal bronchioles [2]. This section of the lungs is responsible for the transport of air to the respiratory zone, so it forms the anatomic dead space [3]. After the terminal bronchioles, the respiratory zone starts with respiratory bronchioles and ends with the alveolar sacs ($j = 23$) [2]. The respiratory zone is the part of the lung, where gas exchange occurs in the alveoli.

Airway closure can occur due to a Plateau-Rayleigh instability when the ASL is too thick. This phenomenon can be observed in healthy conditions whenever the lung volume is low and in diseased conditions, such as asthma, pulmonary edema, and respiratory distress syndrome [4]. Gauglitz and Radke [5] stated that for a clean rigid pipe, lined with a single-layer liquid, the critical thickness to observe coalescence is $h_c^*/a^* \approx 0.12$, where h_c^* is the critical thickness of the liquid film and a^* is the radius of the pipe. Halpern and Grotberg [6,7] investigated the stability of a liquid film lining an airway tube by considering the wall elasticity and surfactants. They concluded that the increasing wall compliance decreases h_c^* , while surfactants increase it. Later, Halpern and Grotberg [8] analyzed the effects of an oscillatory core flow on more viscous liquid film coating a rigid cylinder. They found that the core flow can avoid liquid plug formation in a nonlinear fashion by spreading back and forth the ASL. That is what they termed “reversing butter knife effect.” Additionally, a *compliant collapse* can also be observed in certain situations, where fluid-elastic instabilities arise [9]. If there is a liquid bridge formation without a structural collapse, it is called *film collapse* [10].

For about the first 16 generations, ASL is a bilayer, where the sublayer is serous (serum) and the top layer is mucus [11]. Although the serum predominantly shows Newtonian characteristics, airway mucus is often reported as a highly non-Newtonian substance [12–14]. About 90–95% of airway mucus comprises of water, and it is followed by high-molecular mucin glycoproteins with 2–5% [15]. It additionally includes fractional amounts of lipids, salts, DNA, and cell debris [15]. This mixture of materials gives airway mucus its structured form and thus its non-Newtonian features [13].

The solid content of airway mucus is responsible for its viscoelastic and viscoplastic characteristics. It was shown by Hill *et al.* [16] that these characteristics are directly proportional to the amount of solid in mucus and consequently pulmonary diseases. For example, while solid concentration for a normal pulmonary mucus is around 2 wt%, for a sample from a chronic obstructive pulmonary disease (COPD) patient, it is almost 4%, and it can even go as high as 8% for a cystic fibrosis (CF) patient [16]. Also Lafforgue *et al.* [17] correlated the rise in the solid concentration to the increase of viscoplastic and shear-thinning features by fitting a Herschel-Bulkley model to their steady-state data. This abnormal increase in the viscoelastic and viscoplastic characteristics is usually followed by an increase in viscosity levels as well, and mucociliary clearance can eventually be compromised

[18]. A direct result of this is the growth in the number of bacterial pathogens [13]. Additionally, COPD, CF, and asthma can cause a mucus hypersecretion and obstruct the airway in lethal degrees [18].

Rheology of the airway mucus samples obtained from healthy [19,20] and diseased subjects [19,21–23] has also been studied extensively in the literature. These investigations provided strong indications about viscoelasticity, viscoplasticity, and shear-thinning features and thus elastoviscoplasticity of the pulmonary mucus. Elastoviscoplastic (EVP) fluids can be seen in many areas of our lives from industry to nature. This fluid behavior involves a critical stress (yield stress), above which material starts to flow and below which the behavior of the material is similar to that of an elastic solid [24]. The existence of the yield stress causes a singularity in the deformation of the material, and methods such as viscosity regularization, the augmented Lagrangian method, and mapping of the yield surface to a fixed boundary have been used to overcome the resulting difficulties in modeling [25].

Although simplified viscoplastic constitutive models have been extensively used in the literature, behaviors of most of the real fluids cannot be described solely using variants of these models. For example, the particle settling experiments on well-characterized yield-stress fluids [26–28] showed that the fore-aft symmetry of the flow field, which was observed in the experiments with Newtonian fluids and simulations with classical viscoplastic model assumptions, was lost [29]. Yield stress fluids exhibited a flow asymmetry and a negative wake, i.e., an upward motion of the fluid in the particle's wake. This demonstrated that yield-stress fluids are rather more complex because of their thixotropy and elasticity [28].

In order to include viscoelastic effects that is observed in some viscoplastic fluids, de Souza Mendes [30] suggested a modification of lower-convected Jeffreys liquid, where viscosity, relaxation time, and retardation time are functions of the deformation rate. When the material yields, the proposed constitutive equation reduces to the generalized Newtonian liquid constitutive equation. Otherwise, the model reduces to the Jeffreys liquid constitutive equation. Bénito *et al.* [31] developed a fully tensorial continuous framework to describe the behavior of soft materials, which deform substantially before yielding. After yielding, the material flows as a viscoelastic fluid. In their work, where they studied the oscillatory pipe flow of a Carbopol solution, Park and Liu [32] both carried out experiments to obtain the velocity fields and compared the results with the computational solutions based on the EVP model that they proposed. They used an elastoviscoplastic rheological model, where an elastic spring is serially connected to a regularized Bingham viscoplastic model and found a good agreement with the experimental findings. Belblidia *et al.* [33] proposed another constitutive law to take the elastoviscoplasticity into account. In their model, they built on the model of Papanastasiou [34], and to include the viscoelastic effects, they used the Oldroyd-B model [35].

Based on the thermodynamic theory, Saramito [24] proposed a three-dimensional (3D) constitutive model, which combines the Bingham viscoplastic and the Oldroyd-B viscoelastic models. Accordingly, the behavior of the material is a viscoelastic solid before yielding, and when the stress exceeds a critical level, the material behaves as a viscoelastic fluid. Here the von Mises criterion is used to monitor the yielding. Later, this model is improved to include the shear-thinning behavior by combining the Oldroyd viscoelastic and Herschel-Bulkley models [36]. Recently, Fraggedakis *et al.* [25] compared five constitutive models (three variations of Saramito [24], Park and Liu [32], and Belblidia *et al.* [33]) by performing series of tests, such as simple-shear, uniaxial elongation, and large amplitude oscillatory tests and found that the Saramito variants outperformed the other two models.

Liquid plug formation, propagation, and rupture exert potentially lethal mechanical stresses to the airway wall, where airway epithelium lies [37–40]. The pre-coalescence dynamics of the airway closure in a rigid tube lined by a single-layer Newtonian fluid has been studied experimentally and numerically by Bian *et al.* [41] and Tai *et al.* [42], respectively. They both concluded that mechanical stresses may reach to the levels marked dangerous for the airway epithelium by Bilek *et al.* [37] and Huh *et al.* [39] during the plug formation. Later, Romanò *et al.* [43] investigated the whole closure process, including the postclosure dynamics, by modeling the ASL as a single-layer Newtonian

liquid film. They deduced that stress peaks occurring just after the coalescence, during *bifrontal plug growth*, are responsible for high mechanical stresses exerted on the pulmonary epithelium. The effects of the complex characteristics of the airway mucus on pre-coalescence dynamics were taken into account by Halpern *et al.* [44] using lubrication approximations. In their study, they modelled the ASL as a one-layer Oldroyd-B fluid and analyzed the effect of the Weissenberg number, Wi , on the growth rate of the instabilities and the wall shear stress levels. Romanò *et al.* [45] recently considered viscoelastic effects in a similar problem by using Oldroyd-B and FENE-CR models. They showed that mucus viscoelasticity is responsible for the second peak of the wall shear stress occurring after the coalescence, and this secondary peak can be as extreme as the first one for high Laplace and Weissenberg numbers in a physiological range. Instability of an axisymmetric layer of viscoplastic Bingham liquid coating the interior of a rigid tube is studied by Shemilt *et al.* [46]. This model represents the airway and takes into account the yield stress of mucus. Using long-wave theory, they derived an evolution equation for the thickness of the liquid layer. They found that as the capillary Bingham number increases, the critical layer thickness required to form a liquid plug also increases. Recently, Erken *et al.* [47] studied this problem in a two-layer setting, where both layers were Newtonian. The main findings were the enhanced instability of the system leading to a sooner closure and the damping of the stresses, both of which were related to the existing of the bottom (serous) layer. Moreover, the non-Newtonian effects of mucus have been studied in plug propagation and rupture both numerically and experimentally [48–52], and it has been reported that these features should be considered in airway models.

Airway mucus is a very complex material and exhibits a wide range of non-Newtonian characteristics, such as viscoelasticity, viscoplasticity, shear-thinning, and thixotropy [12]. Therefore, a mucus model that incorporates these features is needed to obtain more realistic results for the airway closure. In this paper, the effects of the non-Newtonian characteristics of pulmonary mucus on the airway closure problem have been investigated using the Saramito-HB model [36]. This constitutive law is a combination of Oldroyd-B and Herschel-Bulkley models, with a power-law index $n > 0$. The model parameters are determined by following a parameter fitting procedure similar to that of Fragedakis *et al.* [53] using the experimental results of Patarin *et al.* [19] for the healthy, asthma, COPD, and CF airway mucus. To compare different pathological conditions of the pulmonary mucus in different settings, extensive simulations are performed for varying surface tension and initial liquid layer thickness. Here we study the airway closure problem in a single-layer setting in order to isolate the effects of the EVP features of the mucus on the closure time and the wall mechanical stresses. The system is further simplified by neglecting the wall deformation and the surfactants. A similar framework was studied by Romanò *et al.* [45], where the liquid lining was a viscoelastic fluid but they considered only the healthy conditions. Here we also include viscoplastic and shear-thinning properties of mucus by utilizing the Saramito-HB model. To the authors' knowledge, effects of the mucus elastoviscoplasticity on airway closure have never been studied so far.

The rest of the paper is organized as follows. Mathematical formulation and numerical method are explained in Sec. II. Then the problem specifications, such as boundary conditions and parameter intervals, are described in Sec. III. Section IV presents the rheological fitting and simulation results by specifically focusing on the effects of different pathological conditions. Finally, the summary and the conclusions of the study are given in Sec. V.

II. FORMULATION AND NUMERICAL METHOD

The governing equations are described in the context of the finite-difference–front-tracking method [54]. Using a one-field formulation, a single set of incompressible momentum and continuity equations is written in the whole computational domain. The interfacial effects are represented as a body force in the momentum equation, and the jumps in the material properties for the different phases are accounted for using an indicator (color) function. The equations are solved in their

dimensional forms denoted by superscript “*”. In the front-tracking framework, the momentum and continuity equations yield

$$\frac{\partial \rho^* \mathbf{u}^*}{\partial t^*} + \nabla^* \cdot (\rho^* \mathbf{u}^* \mathbf{u}^*) = -\nabla^* p^* + \nabla^* \cdot \mu_{l,S}^* (\nabla^* \mathbf{u}^* + \nabla^{*T} \mathbf{u}^*) + \nabla^* \cdot \boldsymbol{\tau}^* \quad (1)$$

$$+ \int_{A^*} \sigma^* \kappa^* \mathbf{n} \delta(\mathbf{x}^* - \mathbf{x}_f^*) dA^*,$$

$$\nabla^* \cdot \mathbf{u}^* = 0, \quad (2)$$

where t^* is the time; \mathbf{u}^* is the velocity vector; p^* is the pressure field; ρ^* and $\mu_{l,S}^*$ are the discontinuous density and solvent viscosity fields, respectively; and $\boldsymbol{\tau}^*$ represents the extra stress tensor. Note that $\mu_l^* = \mu_{l,S}^* + \mu_{l,P}^*$, where $\mu_{l,P}^*$ and μ_l^* are the polymer and total viscosities of the liquid layer, respectively. The effect of the surface tension is represented as a body force in the last term on the right-hand side of Eq. (1), where σ^* is the surface tension coefficient, κ^* is twice the mean curvature, \mathbf{n} is a unit vector normal to the interface, and A^* is the surface area. The surface tension acts only on the interface as indicated by the Dirac delta function δ , whose arguments \mathbf{x}^* and \mathbf{x}_f^* are the points at which the equation is evaluated and the point at the interface, respectively. The gravitational effects are negligible within the asymptotic limit of a small Bond number, i.e., $\text{Bo} = g^* a^{*2} \Delta \rho^* / \sigma^* \ll 1$, where g^* is the gravitational acceleration and $\Delta \rho^*$ is the difference between mucus and air densities. Since the airway flow of interest in the present study falls in such a regime, the gravitational effects are neglected in Eq. (1).

The liquid layer is represented as a Saramito-HB fluid [36]. The EVP equations are solved using the log-conformation method [55]. The extra stresses appearing in Eq. (1) are related to the conformation tensor, \mathbf{B} , that evolves by

$$\left(\frac{\partial \mathbf{B}}{\partial t^*} + \mathbf{u}^* \cdot \nabla \mathbf{B} - \mathbf{B} \cdot \nabla \mathbf{u}^* - \nabla \mathbf{u}^{*T} \cdot \mathbf{B} \right) = \frac{F}{\Lambda^*} (\mathbf{I} - \mathbf{B}), \quad (3)$$

where Λ^* is the relaxation time. In the Saramito-HB model, the relaxation time and the polymeric viscosity are given as $\Lambda^* = \mu_{l,P}^* / G^*$ and $\mu_{l,P}^* = K^* (L^* / U^*)^{(1-n)}$, respectively, where L^* , U^* , G^* , n , and K^* are characteristic length and velocity scales, elastic modulus, power-law index, and consistency parameter, respectively [36]. The Saramito-HB model can be represented by setting the parameters of Eq. (3) to $\mathbf{B} = \boldsymbol{\tau}^* \Lambda^* / \mu_{l,P}^* + \mathbf{I}$ and $F / \Lambda^* = G^* \max[0, \frac{|\boldsymbol{\tau}^{*d}| - \tau_y^*}{K^* |\boldsymbol{\tau}^{*d}|^n}]^{\frac{1}{n}}$ [55,56], where τ_y^* is the yield stress and $\boldsymbol{\tau}^{*d}$ is the deviatoric part of the stress tensor, and its magnitude is given as

$$|\boldsymbol{\tau}^{*d}| = \left(\frac{1}{2} \tau_{ij}^{*d} \tau_{ij}^{*d} \right)^{\frac{1}{2}}. \quad (4)$$

Once the conformation tensor is obtained from Eq. (3), the extra stress tensor is then computed as $\boldsymbol{\tau}^* = \frac{\mu_{l,P}^*}{\Lambda^*} (\mathbf{B} - \mathbf{I})$. Also, it is assumed that the material properties remain constant following a fluid particle, i.e.,

$$\begin{aligned} \frac{D\rho^*}{Dt^*} = 0, \quad \frac{D\mu_{l,S}^*}{Dt^*} = 0, \quad \frac{DG^*}{Dt^*} = 0, \\ \frac{D\tau_y^*}{Dt^*} = 0, \quad \frac{Dn}{Dt^*} = 0, \quad \frac{DK^*}{Dt^*} = 0, \end{aligned} \quad (5)$$

where $D/Dt^* = (\partial/\partial t^*) + \mathbf{u}^* \cdot \nabla^*$ is the material derivative. The material properties vary discontinuously across the interfaces and are given, for example, for density ρ by

$$\rho^* = \rho_g^* I(r, z, t) + \rho_l^* [1 - I(r, z, t)], \quad (6)$$

where the subscripts “g” and “l” denote the properties of the air core and the liquid layer, respectively, and I is the indicator function having the values $I = 0$ in the liquid layer and $I = 1$ in the air

core. All the other material properties, given in Eq. (5), are distributed in the same way across the computational domain depending on the value of I .

The flow equations are written and solved in the context of the front-tracking or finite-difference method [54]. This method contains two grids that are a stationary staggered Eulerian grid, where the flow equations are solved to obtain the velocity, pressure, and extra stress fields, and a Lagrangian grid, which is formed by marker points. The piece of the interface between two neighboring marker points forms a front element. Both the marker points and the front elements are connected to form the air-liquid interface. The material properties are distributed according to the location of the interface (front) at the beginning of each time step according to Eq. (6). To compute the surface tension at the centroids of the front elements, a third-order Legendre polynomial fit is used. Then the surface tension is distributed smoothly onto Eulerian grid points to be added to the momentum equations as a body force to account for the interfacial effects. At each time step, the local flow velocity of the front is interpolated from the Eulerian grid, and the front is moved accordingly. The communication between the Eulerian and the Lagrangian grids are accomplished by using Peskin's cosine distribution function [57].

To approximate the spatial derivatives, central differences are used, except for the convective term in Eq. (3), where a fifth-order WENO-Z method is used. Time integration is accomplished by the projection method developed by Chorin [58]. The method is first-order accurate in time, but a second-order accuracy can easily be achieved by a predictor-corrector scheme as described by Tryggvason *et al.* [59]. However, Muradoglu *et al.* [60] noted that for the first-order method in use, the time-stepping error is smaller compared to the spatial error due to the tight restrictions of the stability condition on the time step for the flow of interest in this study. Hence, the first-order method is here employed.

The extra stress is calculated at each time step and added to the momentum equations to represent the EVP effects [56]. To that end, the generic transport Eq. (3) is solved by changing its parameters for the Saramito-HB model in use. For a detailed explanation of the numerical procedure on how this equation is solved and extra stresses are handled, the reader is referred to Izbassarov and Muradoglu [55].

The indicator function is calculated according to the location of the front at the beginning of each time step as explained in Ref. [59]. For this purpose, a separable Poisson equation, resulting from the divergence of the unit magnitude jumps calculated at the centers of the front elements and distributed onto the neighboring Eulerian grid cells, is solved. Once the indicator function is computed in the whole domain, the material properties are updated according to Eq. (6). Afterwards, the integration is carried out according to these updated properties to obtain the velocity and pressure fields.

The density of marker points in the Lagrangian grid, thus the size of the front elements, is monitored at each time step to prevent numerical inaccuracies and instabilities. Too-coarse a grid can cause poor resolution of the interface, whereas too-dense a grid can cause unwanted wiggles. Therefore, the front elements are kept between prespecified minimum and maximum sizes by splitting large elements by adding new marker points or deleting small elements. During this restructuring of the front, the curvature is considered by using a third-order Legendre interpolation to preserve the smoothness of the interface.

In the front-tracking method, the marker points are explicitly tracked, so the topological change must be implemented by changing the connectivity of the marker points in an appropriate way Tryggvason *et al.* [59]. The procedure suggested by Olgac *et al.* [61] is used in the present study to handle the topological change. Thus, the minimum distance between the interface and the symmetry axis is monitored. When this falls below a prespecified minimum limit, l_{th} , the front element that is closest to the symmetry axis is removed, and the interface is connected to the symmetry axis. The effects of this threshold value, l_{th} , on the results are checked, and it is found that as long as l_{th} is of the order of the Eulerian grid size, the results are uninfluenced.

A detailed information about the front-tracking method can be found in Unverdi and Tryggvason [54], Tryggvason *et al.* [59], and Tryggvason *et al.* [62]. The method has already been validated successfully for an airway closure problem with a Newtonian single-layer case against the results of

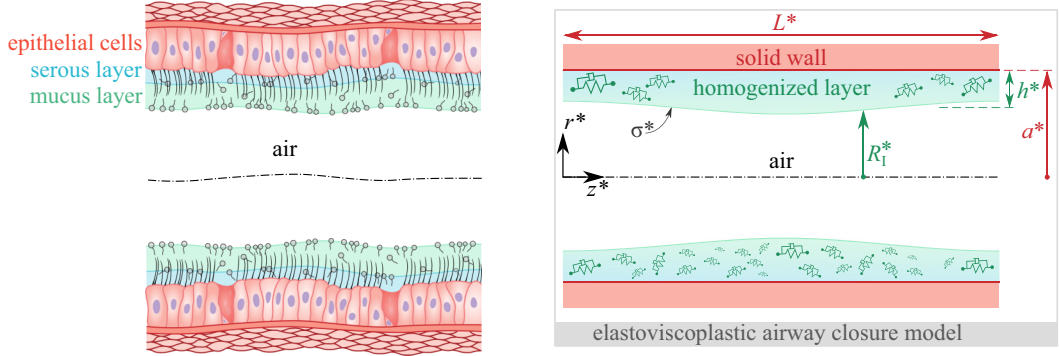


FIG. 1. (Left) The schematic illustration of a part of an airway. (Right) The illustration of the computational domain. The axisymmetric rigid airway wall is lined with the EVP liquid layer, and the liquid layer is surrounded by the air core inside. The length and the radius of the airway lumen is L_z^* and a^* , respectively. The surface tension of the air-liquid interface is σ^* . The radial location of the interface, which is perturbed from its initial state to initiate the instability, is shown by R_l^* .

Romanò *et al.* [43], obtained by using volume-of-fluid (VOF) method and implemented in *basilik* package [63]. The implementation of the Saramito-HB model is first validated against the analytical solution of a single-phase laminar pipe flow given by Chaparian and Tammissola [64]. Saramito-HB model reduces to Oldroyd-B model when $n = 1$ and $\tau_y^* = 0$ [36], so the implementation of the non-Newtonian model is further validated against the results of Romanò *et al.* [45] for the airway closure with a single-layer Oldroyd-B liquid. Although not included here, the results were found to be in good agreement with those of Romanò *et al.* [45].

III. PROBLEM STATEMENT

A schematic of the problem is given in Fig. 1. The airway lumen, whose length and radius are L_z^* and a^* , respectively, is axisymmetric around the centerline, and its wall is rigid. Here the air core is modelled as a Newtonian fluid with constant properties, which are denoted by the subscript “g”. On the other hand, the liquid layer is modelled as an EVP fluid, and its properties are denoted by subscript “l”. The surface tension at the air-liquid interface, σ^* , is assumed to be constant as the other material properties of the air and the liquid film. The computational domain is periodic at $z^* = 0$ and $z^* = L_z^*$, and no-slip boundary conditions are applied at the rigid wall. The liquid layer is perturbed from its initial location, h^* , to initiate the instability, and the radial location of the interface is given by

$$r^* = R_l^* = a^* - h^*[1 - 0.1 \times \cos(2\pi z^*/L_z^*)], \quad (7)$$

where R_l^* is the radial location of the air-liquid interface and z^* and r^* are the axial and radial coordinates, respectively.

The equations are solved in their dimensional form, as mentioned above, and the results are presented in terms of nondimensional groups by making use of a capillary scaling, i.e., length, time, velocity, and stresses are nondimensionalized by a^* , $\mu_{l,S}^* a^*/\sigma^*$, $\sigma^*/\mu_{l,S}^*$, and σ^*/a^* , respectively. The resulting nondimensional parameters can be summarized as

$$\begin{aligned} \text{La} &= \frac{\rho_l^* \sigma^* a^*}{\mu_{l,S}^* 2}, & \text{Bi} &= \tau_y^* = \frac{\tau_y^* a^*}{\sigma^*}, & G &= \frac{G^* a^*}{\sigma^*}, & \text{Wi} &= \frac{\Lambda^* \sigma^*}{a^* \mu_{l,S}^*}, \\ \rho &= \frac{\rho_g^*}{\rho_l^*}, & \mu &= \frac{\mu_g^*}{\mu_{l,S}^*}, & \epsilon &= \frac{h^*}{a^*}, & \lambda &= \frac{L_z^*}{a^*}, \end{aligned} \quad (8)$$

where La , τ_y , G , ρ , μ , ϵ , and λ denote Laplace number, nondimensional yield stress, nondimensional elastic modulus, gas-to-liquid density ratio, gas-to-liquid viscosity ratio, nondimensional initial film thickness, and airway tube length-to-radius ratio, respectively; Bi is the Bingham number and Wi is the Weissenberg number. Also $\mu_{l,s}^*$ and μ_g^* are the liquid solvent viscosity and the total gas viscosity, respectively, and $\mu_l^* = \mu_{l,s}^* + \mu_{l,p}^*$, where μ_l^* is the total liquid viscosity and $\mu_{l,p}^*$ is the polymeric viscosity. In the Saramito-HB model, the relaxation time is defined as $\Lambda^* = \mu_{l,p}^*/G^*$. Here $\mu_{l,p}^* = K^*(\frac{L^*}{U^*})^{1-n}$, where L^* is the length scale and U^* is the velocity scale.

The parameter ranges are determined to represent the 9th-to-10th generation of a typical adult human lung. The airways can be compared to branching tubular trees, and the radii of these tubes decrease at each generation [1]. The airway closure starts to be seen after 9th or 10th generation because airway radii are not small enough in the earlier ones [65,66]. Thus, here, the airway radius is taken as $a^* = 0.065$ cm [67]. Also, it should be noted that a typical airway lumen has a length-to-radius ratio of $\lambda = 6$ [68], so this value is used throughout this paper.

For a Newtonian one-layer liquid lining a clean rigid pipe, the liquid plug formation starts to occur when $h_c^*/a^* \geq 0.12$, where h_c^*/a^* is the critical initial film thickness [5]. Accordingly, in this study, the initial nondimensional film thickness, ϵ , is varied in the range of $0.25 \leq \epsilon \leq 0.35$ to describe different intensities of mucus hypersecretion.

Romanò *et al.* [43] stated that the density of the single-layer liquid can be taken as $\rho_l^* = 1000$ kg/m³. Also, the solvent viscosity of the liquid layer is fixed at $\mu_{l,s}^* = 0.013$ Pa s [42]. On the other hand, to represent the surfactant-deficient conditions, three different surface tension values are used, $\sigma^* = 0.026$ N/m, $\sigma^* = 0.052$ N/m, and $\sigma^* = 0.078$ N/m corresponding to $La = 100$, $La = 200$, and $La = 300$, respectively [69,70].

The properties of the airway mucus are determined for the healthy, asthma, CF, and COPD cases using the experimental data of Patarin *et al.* [19] to examine the effects of the pathological conditions on the airway closure phenomenon. The EVP parameters of the liquid layer for these conditions are extracted using a nonlinear regression, as explained in detail in Sec. IV A.

After the healthy, asthma, COPD, and CF conditions are compared, a parametric study is carried out to see the effects of individual parameters of the Saramito-HB model. For this purpose, the healthy case is taken as the baseline, and the elastic modulus G^* , the yield stress τ_y^* , and the shear-thinning index n are varied in a physiologically meaningful range. Hu *et al.* [49] stated that G^* can reach up to $G^* \approx 200$ Pa depending on the pathological conditions and the angular frequency. In another study, they studied the plug rupture problem numerically by modeling the liquid film as a Herschel-Bulkley fluid [50], where they varied τ_y^* up to the extreme conditions $\tau_y^* = 100$ Pa. Based on the work of Lafforgue *et al.* [17], n can also vary depending on the solid concentration of mucus. By fitting a Herschel-Bulkley model to their experimental data on a mucus simulant proposed by Zahn *et al.* [71], they found that $0.37 \leq n \leq 0.78$. Therefore, in our parametric study, which is omitted in this paper for brevity, the elastic modulus G^* , yield stress τ_y^* , and power-law index n are studied in the ranges of $G^* \in [0.094, 100]$ Pa, $\tau_y^* \in [0.04, 100]$ Pa, and $n \in [0.4, 1.0]$. In terms of the nondimensional quantities, these lead to $G \in [0.0013, 2.5]$, $\tau_y \in [0.01, 2.5]$, and $n \in [0.4, 1.0]$. The rheological fitting for these parameters (explained in Sec. IV A) is performed within these ranges as well.

IV. RESULTS AND DISCUSSION

First, the effects of pathological conditions of mucus are studied. In Sec. IV A, a parameter fitting algorithm (similarly to Fragedakis *et al.* [53]) is followed to obtain the parameters of the Saramito-HB model for healthy, asthma, COPD, and CF mucus based on the experimental data of Patarin *et al.* [19]. Afterwards, these mucus states are compared by varying ϵ and La to represent different intensities of mucus hypersecretion and surfactant deficiency. Finally, a parametric study is performed on the healthy mucus to see the individual effects of the parameters.

The computational domain is given in Fig. 1, and it has an axial length of $L_z^* = 6a^*$ and a radial length of a^* . A uniform tensor-product structured grid is used in all simulations carried out. Grid

convergence is checked, and it is found that a stretched Cartesian grid of 96×576 is enough to reduce the spatial errors below 4%, for the wall shear stress excursion, $\Delta\tau_w = \max(\tau_w) - \min(\tau_w)$, the wall pressure excursion, $\Delta p_w = \max(p_w) - \min(p_w)$, and the minimum core radius, R_{\min} . The grid is stretched so that the radial grid size, Δr , is three times smaller at the wall compared to the grid near the centerline.

A. Determination of rheological properties

In this section, the Saramito-HB model is fitted to the experimental data provided by Patarin *et al.* [19], and the model parameters for the Saramito-HB model are obtained. In their set of experiments, they collected mucus samples from healthy, asthma, COPD, and CF subjects and analyzed them in a quite large strain amplitude interval by fixing the frequency to 0.6 Hz. Moreover, they presented the evolution of elastic modulus (G') and viscous modulus (G'') by varying strain amplitude in a large interval and concluded that these four different conditions have distinct rheological behaviors.

First, the Saramito-HB constitutive law is written in its 1D form as Fraggedakis *et al.* [25] suggested

$$\frac{1}{G^*} \overset{\nabla}{\boldsymbol{\tau}^*} + \max \left[0, \frac{|\boldsymbol{\tau}^{*d}| - \tau_y^*}{K^* |\boldsymbol{\tau}^{*d}|^n} \right]^{\frac{1}{n}} \boldsymbol{\tau}^* = 2\mathbf{D}^*, \quad (9)$$

where G^* , τ_y^* , n , and K^* are the elastic modulus, the yield stress, the power-law index, and the consistency parameter, respectively. $|\boldsymbol{\tau}^{*d}|$ is the magnitude of the deviatoric part of the extra stress tensor, $\boldsymbol{\tau}^*$, and its definition is given in (4). The symbol “ ∇ ” above $\boldsymbol{\tau}^*$ denotes the upper-convected Maxwell derivative, and, finally, \mathbf{D}^* is the deformation tensor, which is defined as $\mathbf{D}^* = \frac{1}{2}[(\nabla^* \mathbf{u}^*) + (\nabla^* \mathbf{u}^*)^T]$. According to Eq. (9), the material exhibits a shear-thinning behavior when $0 < n < 1$ and an unusual shear-thickening behavior when $n > 1$ [36].

Then the equation is solved according to its simple shear solution. In LAOStrain, strain-controlled Large amplitude oscillatory shear (LAOS) test [72,73], the input strain is given by

$$\gamma = \gamma_o \sin(\omega^* t^*), \quad (10)$$

where ω^* is the input angular frequency. However, it should be noted that the Saramito-HB model does not take the strain as an input, so the strain rate is defined as $\dot{\gamma} = \partial_t \gamma$ and it is computed by taking the time derivative of the strain input. The input velocity field is defined as the simple shear flow

$$\mathbf{u}^* = (\dot{\gamma}^*(t^*)y^*, 0, 0) \quad (11)$$

Before starting with the nonlinear regression, the yield stress, τ_y^* , of the material is obtained by a method proposed by Yang *et al.* [74]. This method suggests that the in-phase stress component is given by $\tau' = G' \gamma_o$. When this stress component is plotted against the varying strain amplitudes, the maximum value that the in-phase stress component attains is the yield stress of the material, i.e., the stress, at which structural breakdown occurs. The variation of τ' by $\gamma_o\%$ is given in Fig. 2. The yield stresses found following this method are given in Table I. After the yield stresses are obtained for the four types of mucus samples, then the fitting is done for the remaining three parameters (G^* , n , and K^*). Note that for the COPD case, there is not a conclusive yield stress from this method, so for this condition of mucus, the yield stress value is taken from Table 2 of Patarin *et al.* [19] (σ_c for COPD, spontaneous case, where no induction is necessary for patients to expectorate sputum).

For the fitting procedure, a cost function is used to determine the best possible fitting to the experimental data. As the cost function, a modified version of Fraggedakis *et al.* [53] is used, which is

$$\text{Cost}(G^*, n, K^*) = \sum_{i=1}^M \left(\left[\frac{G'_{\text{fit}}}{G'_{\text{exp}}} - 1 \right]^2 + \left[\frac{G''_{\text{fit}}}{G''_{\text{exp}}} - 1 \right]^2 \right), \quad (12)$$

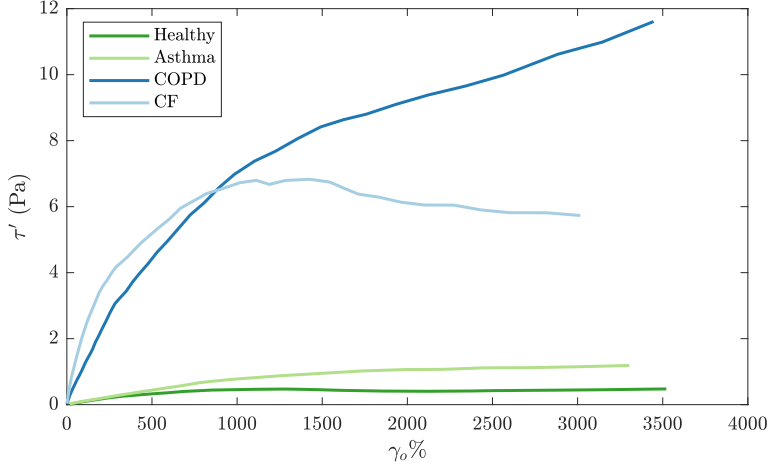


FIG. 2. The in-phase stress component vs. strain amplitude, γ_o for healthy, asthma, COPD, and CF mucus.

where M is the number of strain amplitude values measured for each mucus condition.

The steps of the fitting algorithm can be summarized as follows:

- (1) Initial G^* , n , and K^* are assumed (τ_y^* is determined beforehand, as explained above).
- (2) At each strain amplitude, the resulting stress response is analyzed by using Fourier transform rheology.
- (3) G' and G'' are obtained for the assumed model parameters and the given strain amplitude.
- (4) The cost value is calculated from (12).
- (5) If the cost function reaches its local minimum, then the algorithm stops and G^* , n , and K^* are obtained. Otherwise, the values at the first step are modified and the algorithm runs until a local minimum is reached. To solve this minimization problem Matlab's [75] "fmincon" function is used.

The results of the fitting processes for the four conditions (healthy, asthma, COPD, and CF) are given in Table I. It is clearly seen that the CF mucus displays the most elastic characteristics in contrast with the healthy mucus. The experiments on mucus simulants [17] and real mucus collected

TABLE I. The parameters of the Saramito-HB model determined by performing a rheological fitting procedure to the experimental results of Patarin *et al.* [19].

	Healthy	Asthma	COPD	CF
G^* (Pa)	0.094	0.105	1.155	2.109
τ_y^* (Pa)	0.476	1.186	11.77 ^a	6.830
n	0.552	0.331	0.752	0.513
K^* (Pa s ^{n})	0.124	1.037	1.056	1.701
$G_{La=100}$	2.350×10^{-3}	2.625×10^{-3}	2.887×10^{-2}	5.272×10^{-2}
$G_{La=200}$	1.175×10^{-3}	1.312×10^{-3}	1.444×10^{-2}	2.636×10^{-2}
$G_{La=300}$	7.833×10^{-4}	8.750×10^{-4}	9.625×10^{-3}	1.757×10^{-2}
$W_{iLa=100}$	111.1	141.0	383.8	49.66
$W_{iLa=200}$	162.9	177.3	646.4	70.87
$W_{iLa=300}$	203.8	202.8	876.9	87.26
$Bi_{La=100} = \tau_{y,La=100}$	1.189×10^{-2}	2.965×10^{-2}	2.942×10^{-1}	1.707×10^{-1}
$Bi_{La=200} = \tau_{y,La=200}$	5.950×10^{-3}	1.482×10^{-2}	1.471×10^{-1}	8.537×10^{-2}
$Bi_{La=300} = \tau_{y,La=300}$	3.967×10^{-3}	9.883×10^{-3}	9.808×10^{-2}	5.692×10^{-2}

^aFrom Table 2 of Patarin *et al.* [19] (σ_c for COPD, spontaneous case).

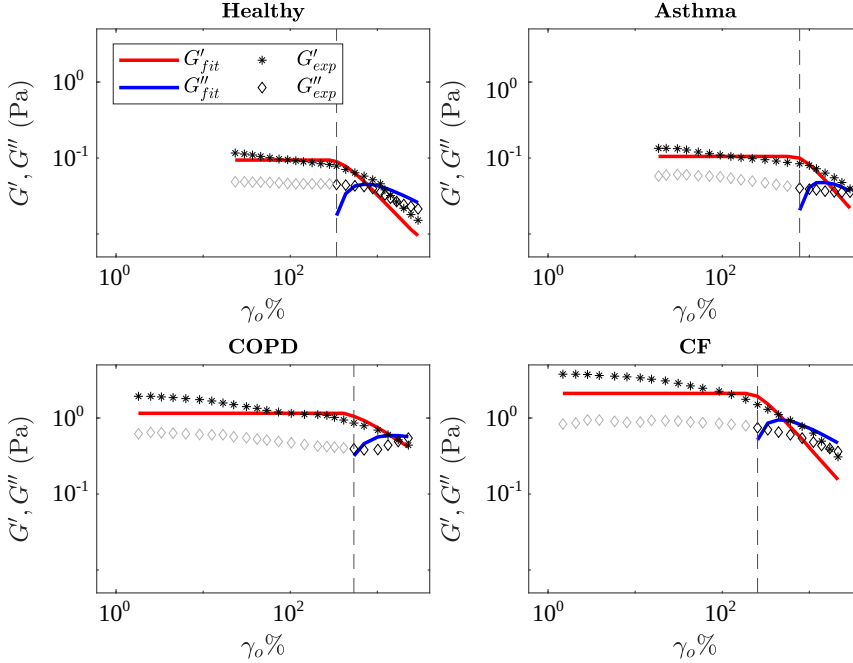


FIG. 3. The viscoelastic moduli, G' and G'' vs. strain amplitude, $\gamma_o\%$ for asthma, healthy, COPD, and CF mucus. The solid lines represent the viscoelastic moduli obtained after performing a parameter fitting to the experimental data of Patarin *et al.* [19], whose results are denoted by symbols. The vertical dashed black line represents the yield strain amplitude for each case.

from subjects [16] have shown that the mucus yield stress increases in the pathological conditions. The present results are consistent with this finding, and they are in line with the critical stresses presented in Patarin *et al.* [19].

The resulting G' and G'' plotted against the strain amplitude, $\gamma_o\%$, are depicted in Fig. 3. As seen from the vanishing G'' and constant G' , the Saramito-HB model predicts an ideal solid response until the material yields. This problem could be alleviated by using a kinematic hardening model, which predicts nonzero G'' prior to yielding [53]. However, as will be shown in the following sections, mucus adherent to the wall already yields just before and after the closure, when stress peaks occur, except extremely high-yield-stress cases (e.g., $\tau_y = 2.5$). Therefore, the kinematic hardening concept is not included in the EVP model in the present study, and this is the reason the markers for G'' are grayed out in the unyielded region in Fig. 3. Furthermore, the experimental results of airway mucus rheology are usually prone to some problems such as saliva contamination [76], effect of hypertonic saline solution (HSS) induction [19], and small quantities of samples that can be obtained [77]. These should be remembered when analyzing such experimental studies on airway mucus samples.

B. Yielded zones for the healthy and the pathological conditions

Table I shows that healthy, asthma, COPD, and CF mucus have different EVP characteristics. G^* and τ_y^* of COPD and CF mucus samples are almost an order of magnitude larger than those of the healthy and asthma cases. Therefore in this section, the yielded zones are compared during an airway closure process of these cases with the parameters obtained in Sec. IV A. In all cases, $\epsilon = 0.35$ and $La = 300$ are chosen to induce airway closure for COPD and CF cases, where otherwise strong EVP characteristics inhibit the growth of the capillary instability that leads to airway closure. To

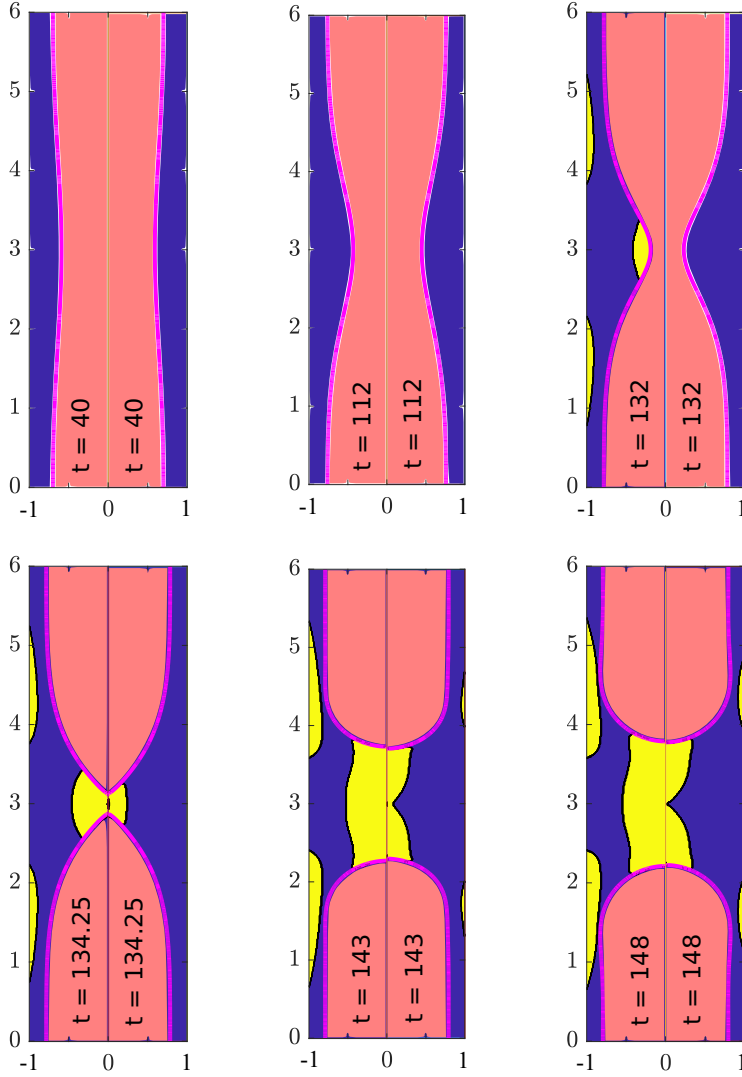


FIG. 4. Comparison of yield zones between healthy (left-hand side of each panel) and asthma (right-hand side of each panel). Air is represented by light red. Yielded and unyielded regions of the liquid layer represented by yellow and blue, respectively. For EVP parameters of the liquid layer, see Table I ($\lambda = 6$, $\epsilon = 0.35$, and $La = 300$).

determine the unyielded regions, a similar logic as Chaparian *et al.* [78] is used, so a criterion of $\max[0, \frac{|\tau^{*d}| - \tau_y^*}{K^* |\tau^{*d}|^n}]^{(1/n)} < 10^{-3}$ is set. The threshold of 10^{-3} is determined so that going lower than that does not alter the results substantially, but it prevents wiggles, which would be caused by the numerical nature of the study.

Figures 4–6 show how yielded and unyielded zones evolve with airway closure. In each figure, the left-hand side is the healthy case, and the right-hand sides are asthma, CF, and COPD cases, respectively. Newtonian air is represented by light red, and yielded and unyielded zones in EVP liquid layer are represented by yellow and blue, respectively. Snapshots are taken to show how yielded zones evolve with the deformation of the air-liquid interface, so there are three snapshots before and three after the closure event for each comparison.

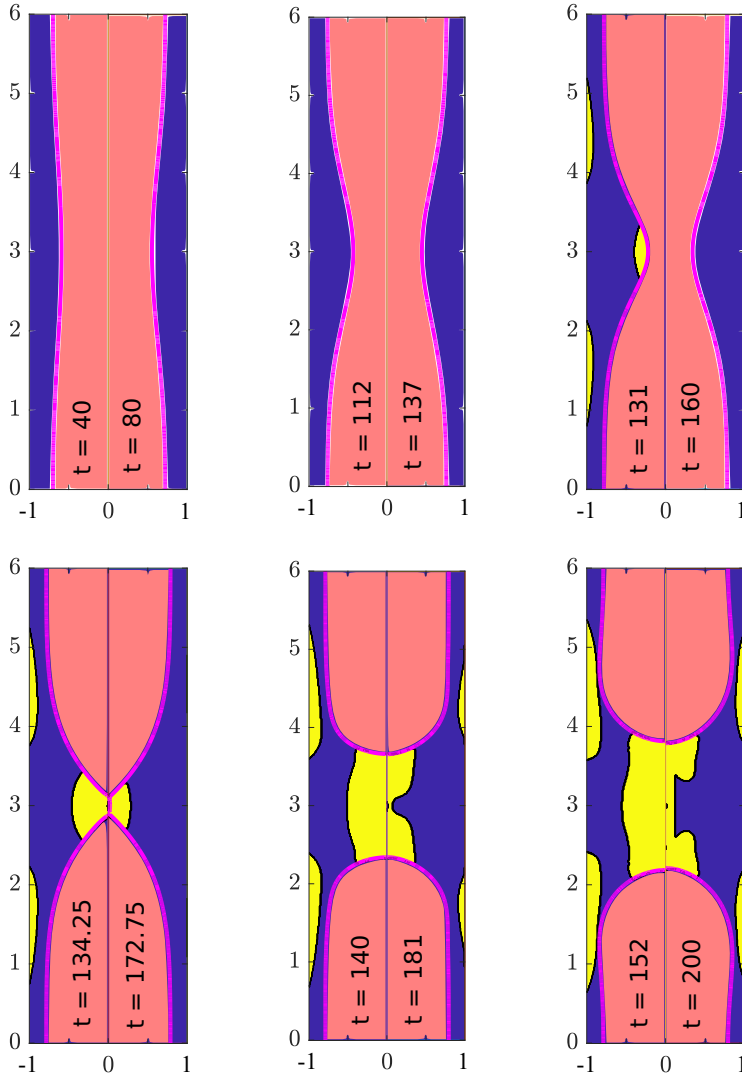


FIG. 5. Comparison of yield zones between healthy (left-hand side of each panel) and COPD (right-hand side of each panel) mucus. Air is represented by light red. Yielded and unyielded regions of the liquid layer are represented by yellow and blue, respectively. For EVP parameters of the liquid layer, see Table I ($\lambda = 6$, $\epsilon = 0.35$, and $La = 300$).

First, the healthy and asthma mucus are compared in Fig. 4. As shown, EVP characteristics of these conditions are closer compared to that of the other two cases. The elastic modulus of the asthma mucus is 11.7% more than that of healthy case, and its yield stress is more than double. Here having a similar G enables them to have almost the same nondimensional closure time (t_c), but due to its higher τ_y , much less mucus yields during the plug formation in the asthma mucus. The EVP liquid layer is mainly in unyielded state especially before the breakup, so the bulk fluid is mainly affected by the elastic behavior and solvent viscosity. Although it could not have been included in this paper due to brevity, this has been confirmed in a parametric study, where τ_y^* and G^* of the material has been individually varied in our parameter range, and it has been found that G^* is the most significant parameter responsible for the closure time. This study has showed that even

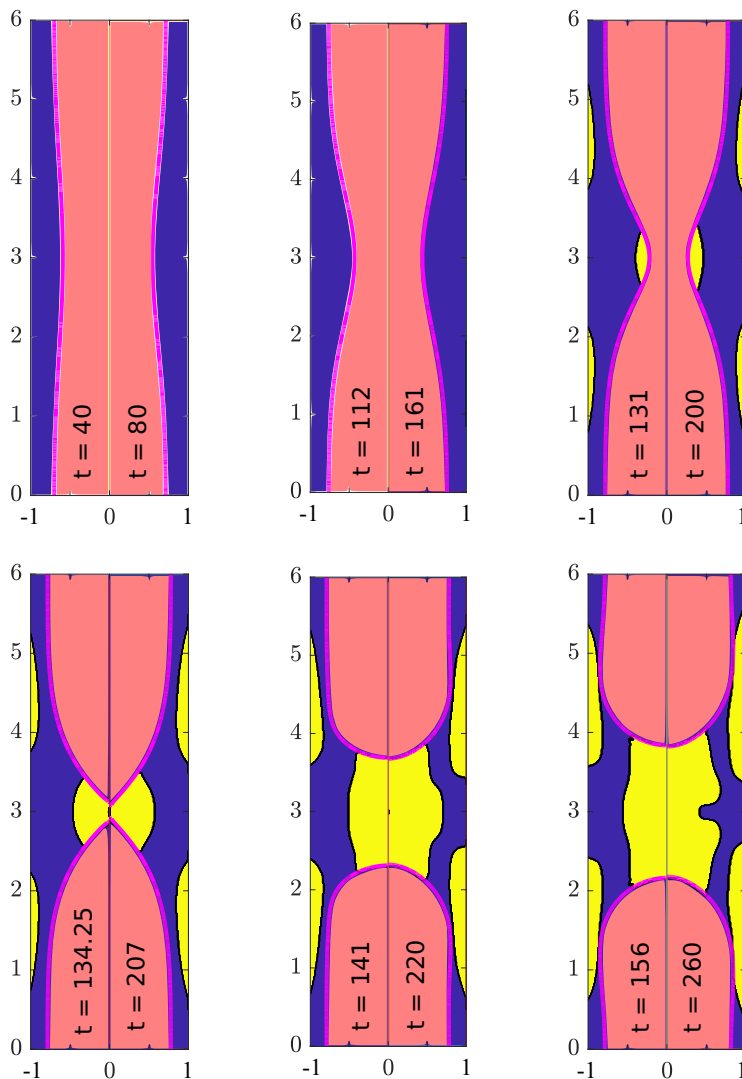


FIG. 6. Comparison of yield zones between healthy (left-hand side of each panel) and CF (right-hand side of each panel) mucus. Air is represented by light red. Yielded and unyielded regions of the liquid layer are represented by yellow and blue, respectively. For EVP parameters of the liquid layer, see Table I ($\lambda = 6$, $\epsilon = 0.35$, and $La = 300$).

for the maximum value of yield stress in our parameter range, the closure occurred with a negligible delay, although there was no yielded regions. The liquid layer was able to bend as an elastic solid when G was not significantly large. Moreover, in both the healthy and asthma cases, yielded zones concentrate at the plug tip and near the wall close to the shoulder, where shear stresses prevail.

Then, the healthy and COPD mucus cases are compared in Fig. 5. The rheological fitting in Sec. IV A resulted in an order of magnitude larger τ_y and G for COPD mucus than healthy one. Larger G of the COPD mucus results in a $\Delta t_c = 38.5$ difference between the nondimensional closure times of these cases due to increased stiffness of the mucus. This finding is consistent with the previous interpretation from Romanò *et al.* [45], where it was shown that Wi has a significant impact on the closure time (note that Wi is inversely proportional to G). Furthermore, the COPD mucus has

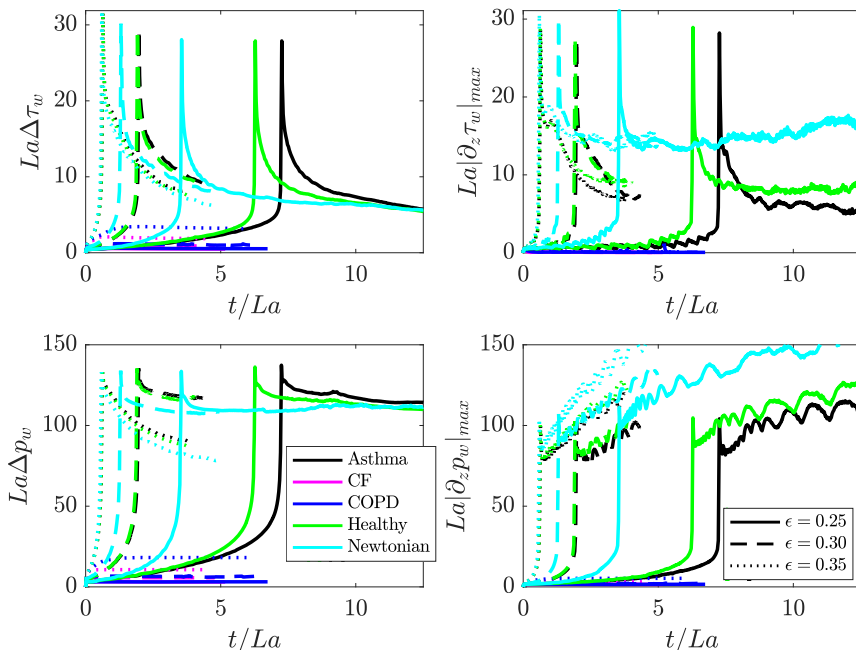


FIG. 7. The effects of pathological conditions for $La = 100$. The initial film thickness ϵ is also varied in each panel. Time evolutions of the wall shear stress excursions $\Delta\tau_w = \max(\tau_w) - \min(\tau_w)$ (top left), the maximum absolute value of the wall shear stress gradient $|\partial_z\tau_w|_{max}$ (top right), the wall pressure excursions $\Delta p_w = \max(p_w) - \min(p_w)$ (bottom left), and the maximum absolute value of the wall pressure gradient $|\partial_z p_w|_{max}$ (bottom right) for asthma (black lines), CF (magenta lines), COPD (blue lines), healthy (green lines), and Newtonian (cyan lines) cases for $\epsilon = 0.25$ (solid lines), $\epsilon = 0.30$ (dashed lines), and $\epsilon = 0.35$ (dotted lines). Note that the nondimensional time t is divided by La to eliminate the effect of surface tension, σ^* , on the time scaling for a better interpretation of the results. The stress excursions and gradients $\Delta\tau_w$, $|\partial_z\tau_w|_{max}$, Δp_w , and $|\partial_z p_w|_{max}$ are also rescaled by La for the same purpose.

smaller yielded zone due to its higher τ_y , and these are located at the bulge tip and just behind the shoulder as in the previous case, since shear stresses are larger in these regions.

Finally, Fig. 6 compares the yielded zones of healthy and CF mucus during the closure. Here the CF mucus behaves somewhat counterintuitively compared to the other cases because despite its larger τ_y , it has a larger yielded zone compared to the healthy case. However, it should be noted that its G is also 82.6% larger than that of the COPD case, so actually the COPD and CF cases have fairly different Weissenberg numbers ($Wi_{CF} = 87.26$ and $Wi_{COPD} = 876.9$, see Table I). Izbassarov and Tammisola [79] presented a complete yielding regime map for an EVP droplet in a Newtonian medium in a certain Wi and Bi interval. They showed that when Wi of the droplet decreases (G increases), it can yield even at higher Bi . Therefore, it would be interesting to further study the interplay between Wi and Bi in yielded regions in this interfacial instability problem.

C. Effect of pathological conditions

The healthy, asthma, COPD, CF, and Newtonian conditions are compared in terms of wall shear stress and pressure excursions and their local gradients. The EVP parameters obtained in Sec. IV A are used to simulate the healthy, asthma, COPD, and CF mucus. Newtonian case is also simulated just to compare how the EVP characteristics of the liquid layer affect the mechanical stresses. Furthermore, ϵ and La are varied to study conditions, such as mucus hypersecretion and surfactant deficiency, and also to induce the closure for highly viscoplastic cases. The results

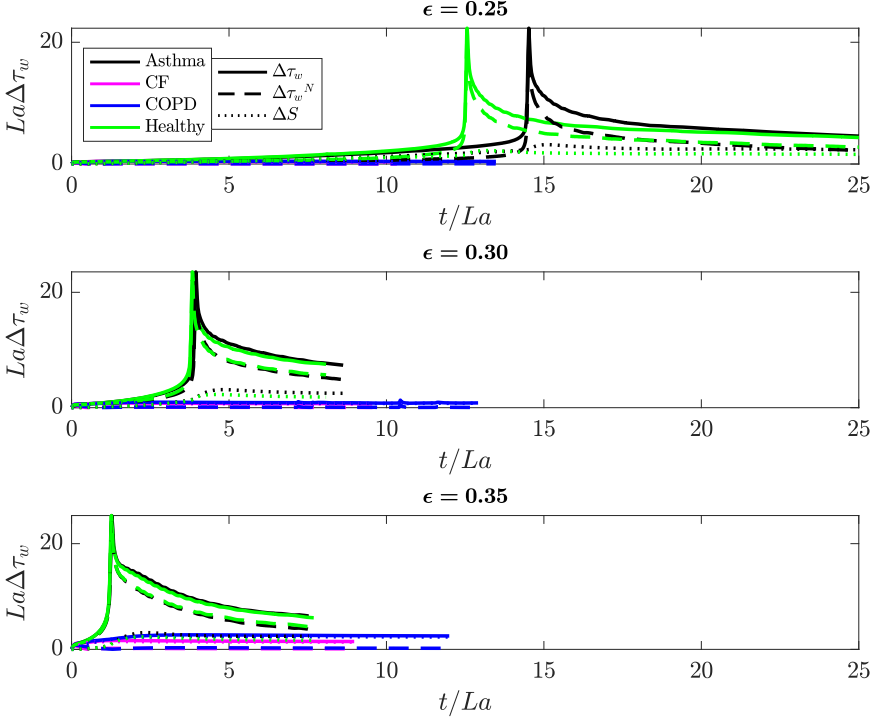


FIG. 8. Evolution of wall tangential stress excursion, $\Delta\tau_w = \max(\tau_w) - \min(\tau_w)$, which consists of Newtonian ($\Delta\tau^N$) and extrastress (ΔS) components, for $La = 100$ and $\epsilon = 0.25$ (top), $\epsilon = 0.30$ (middle), and $\epsilon = 0.35$ (bottom) for asthma (black lines), CF (magenta lines), COPD (blue lines), healthy (green lines), and Newtonian (cyan lines) cases. The wall tangential stress excursion $\Delta\tau_w$ and its Newtonian $\Delta\tau^N$ and extrastress ΔS components are represented by solid, dashed, and dotted lines, respectively. Note that the nondimensional time, t , is divided by La to eliminate the effect of surface tension, σ^* , on the timescaling for a better interpretation of the results. Stress excursion values are also rescaled by La for the same purpose.

of this section are presented in the following three subsections, where $La = 100$, $La = 200$, and $La = 300$, respectively.

I. $La = 100$

The conditions in this section describe a part of an airway with relatively normal surfactant activity with increasingly severe mucus hypersecretion for asthma, CF, COPD, healthy, and Newtonian liquid layers. However, it should be noted that the full surfactant effects are not included in the present study, and the terminology here is intended to represent the surfactant activity in an average sense. We mimic the surfactant effects by varying the mean air-liquid surface tension as a decrease of the mean surfactant concentration (surfactant deficiency) causes an increase in the mean surface tension, hence the Laplace number, La . In Fig. 7, wall tangential and normal stress local gradients, as well as the stress excursions are depicted for $La = 100$ for $\epsilon = 0.25$, $\epsilon = 0.30$, and $\epsilon = 0.35$. Mechanical stresses and nondimensional time (t) are rescaled by La to eliminate the effect of surface tension in the original scaling and to better interpret the results. It is seen that strong EVP features of CF and COPD mucus inhibit airway closure at this La value. The maximum values of the stress peaks for the healthy and asthma cases are almost the same regardless of ϵ , since these initial stress peaks are mostly related to the Newtonian nature of the liquid [45]. We moreover note that t_c moves closer and converges to the Newtonian case in both healthy and asthma cases as ϵ

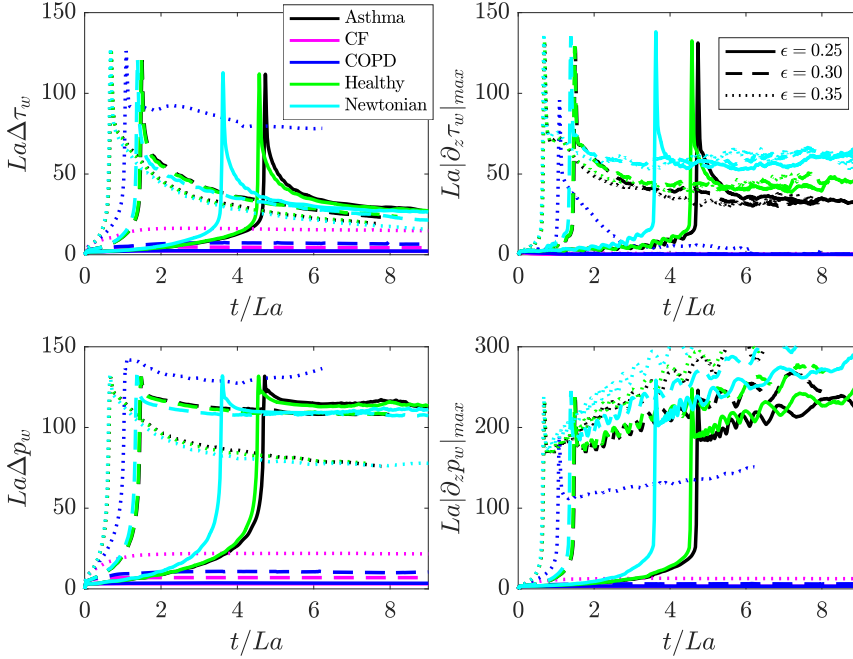


FIG. 9. The effects of pathological conditions for $La = 200$. The initial film thickness ϵ is also varied in each panel. Time evolutions of the wall shear stress excursions $\Delta\tau_w = \max(\tau_w) - \min(\tau_w)$ (top left), the maximum absolute value of the wall shear stress gradient $|\partial_z\tau_w|_{max}$ (top right), the wall pressure excursions $\Delta p_w = \max(p_w) - \min(p_w)$ (bottom left), and the maximum absolute value of the wall pressure gradient $|\partial_z p_w|_{max}$ (bottom right) for asthma (black lines), CF (magenta lines), COPD (blue lines), healthy (green lines), and Newtonian (cyan lines) cases for $\epsilon = 0.25$ (solid lines), $\epsilon = 0.30$ (dashed lines), and $\epsilon = 0.35$ (dotted lines). Note that the nondimensional time t is divided by La to eliminate the effect of surface tension, σ^* , on the timescaling for a better interpretation of the results. The stress excursions and gradients $\Delta\tau_w$, $|\partial_z\tau_w|_{max}$, Δp_w , and $|\partial_z p_w|_{max}$ are also rescaled by La for the same purpose.

increases indicating that the effect of pathological conditions on the closure time diminishes as the initial liquid layer thickness increases.

Shear stress excursion, $\Delta\tau_w$, is decomposed into its extrastress, ΔS , and Newtonian, $\Delta\tau^N$, components in Fig. 8. As it was discussed earlier, the healthy and asthma mucus have weak viscoelastic and viscoplastic characteristics, so except for a minor increase in ΔS after the closure, there is no significant effect of them on the postcoalescence dynamics. Also, initial peak is almost solely due to the Newtonian component, as it was also pointed out by Romanò *et al.* [45].

2. $La = 200$

After studying the airway closure in $La = 100$, the surface tension of the air-liquid interface is increased, and the system is analyzed when $La = 200$. The results are presented in the same fashion as in the previous subsection. Figure 9 shows that closure times for the healthy, asthma, and Newtonian cases are short, and the stresses are higher compared to the $La = 100$ case as expected. However, the biggest difference is that there is a liquid plug formation for the COPD mucus at this condition, but its closure is slower compared to the healthy and asthma cases due to its higher G . Its tangential and normal stress excursion peaks are around the same compared to the other cases, where closure occurs. However, the local gradients of these stresses are significantly lower. This will be discussed in Sec. IV C 4.

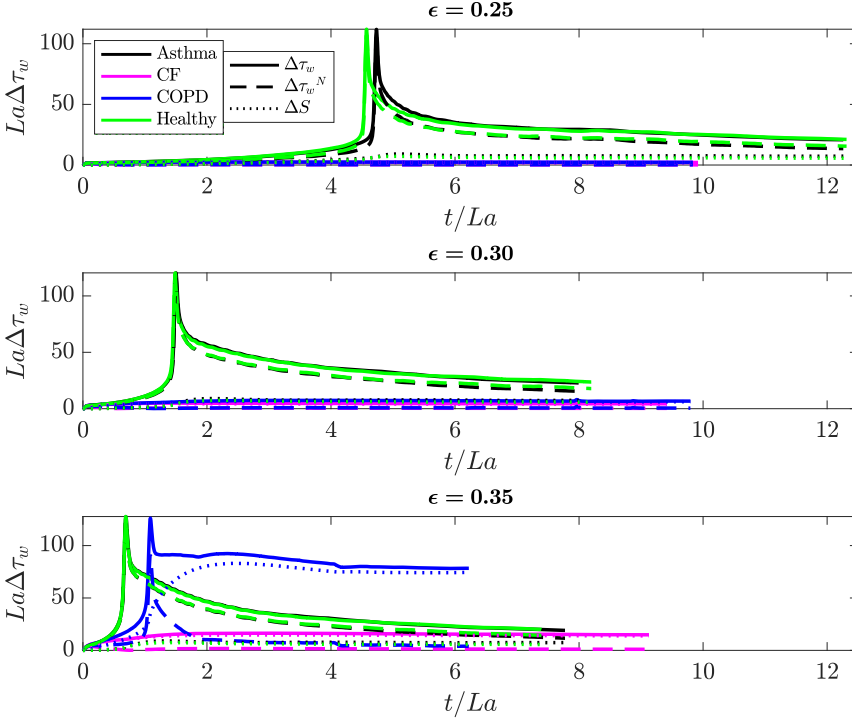


FIG. 10. Evolution of wall tangential stress excursion, $\Delta\tau_w = \max(\tau_w) - \min(\tau_w)$, which consists of Newtonian ($\Delta\tau^N$) and extrastress (ΔS) components, for $La = 200$ and $\epsilon = 0.25$ (top), $\epsilon = 0.30$ (middle), and $\epsilon = 0.35$ (bottom) for asthma (black lines), CF (magenta lines), COPD (blue lines), healthy (green lines), and Newtonian (cyan lines) cases. The wall tangential stress excursion $\Delta\tau_w$ and its Newtonian $\Delta\tau^N$ and extrastress ΔS components are represented by solid, dashed, and dotted lines, respectively. Note that the nondimensional time, t , is divided by La to eliminate the effect of surface tension, σ^* , on the timescaling for a better interpretation of the results. Stress excursion values are also rescaled by La for the same purpose.

The tangential wall stress excursion is decomposed into its Newtonian and extra stress components for this case as well as in Fig. 10. For the less EVP cases (healthy and asthma), the contribution of extra stress to the total $\Delta\tau_w$ is very low as in $La = 100$. However, for the COPD mucus the initial peak increases almost by 30% due to the increase in the extra stress contribution to the total tangential stress excursion on the wall. This indicates that in highly EVP mucus, the peak of the stresses may not be solely due to the Newtonian contribution, but also to the extra stress contribution. The extra stress keeps growing as the Newtonian component relaxes after the closure. Another major point for COPD closure is that extra stress persists after the closure, and its magnitude is around the same levels as the Newtonian peak. This suggests that highly EVP mucus damages the cells on the respiratory wall continuously, which is opposite to the Newtonian case, where the stresses relax to lower levels after reaching their peak values.

3. $La = 300$

To investigate the closure for surfactant-deficient conditions, σ^* is increased further, and the results are presented in Fig. 11. The trends for t_c and the peaks of stresses seen in $La = 200$ case continue for $La = 300$ as well. However, due to the extreme conditions for La and ϵ , the COPD mucus forms a plug at $\epsilon = 0.30$ and $\epsilon = 0.35$, and the CF mucus also forms a plug at $\epsilon = 0.35$. The closure time t_c of the CF mucus is slightly delayed, but its peaks for $\Delta\tau_w$ and Δp_w are around the

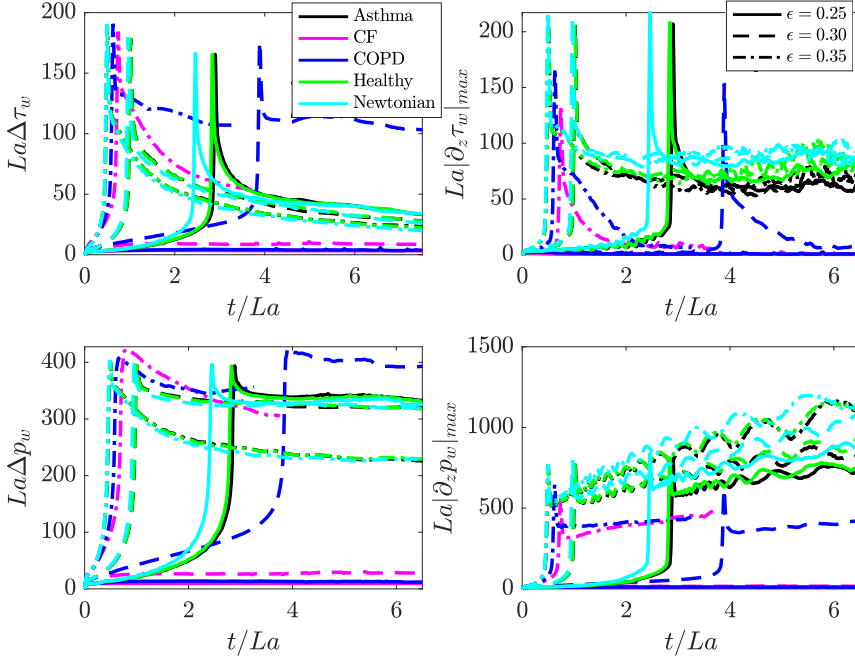


FIG. 11. The effects of pathological conditions for $La = 300$. The initial film thickness ϵ is also varied in each panel. Time evolutions of the wall shear stress excursions $\Delta\tau_w = \max(\tau_w) - \min(\tau_w)$ (top left), the maximum absolute value of the wall shear stress gradient $|\partial_z\tau_w|_{\max}$ (top right), the wall pressure excursions $\Delta p_w = \max(p_w) - \min(p_w)$ (bottom left), and the maximum absolute value of the wall pressure gradient $|\partial_z p_w|_{\max}$ (bottom right) for asthma (black lines), CF (magenta lines), COPD (blue lines), healthy (green lines), and Newtonian (cyan lines) cases for $\epsilon = 0.25$ (solid lines), $\epsilon = 0.30$ (dashed lines), and $\epsilon = 0.35$ (dotted lines). Note that the nondimensional time t is divided by La to eliminate the effect of surface tension, σ^* , on the timescaling for a better interpretation of the results. The stress excursions and gradients $\Delta\tau_w$, $|\partial_z\tau_w|_{\max}$, Δp_w , and $|\partial_z p_w|_{\max}$ are also rescaled by La for the same purpose.

same levels compared to the other cases. Furthermore, tangential and normal local stress gradients are lower as it was seen in Fig. 9 for the COPD mucus.

The extra stress contribution is also checked for the $La = 300$ case in Fig. 12. The results show similar characteristics to the $La = 200$ case. However, there are two important points to note. The first one is that extra stress component almost doubles the initial peak for the CF mucus. After the peak, the stress relaxes very slowly compared to the healthy and asthma conditions. The second point is that the stresses in the CF mucus relaxes unlike the COPD mucus, where extra stress persists for the entire duration of the simulation. The COPD mucus has higher τ_y than that of the CF mucus, therefore it is interpreted that this makes the relaxation of the stresses more difficult, and as a result, the airway epithelial cells are exposed to high levels of stress excursions as long as the plug exists. This phenomenon has not been observed by the viscoelastic simulations of Romanò *et al.* [45], where they reported a secondary peak of the stresses after relaxation from the initial Newtonian peak.

4. Detailed analysis of the lower local stress gradients in the CF and COPD conditions

To further analyze the lower peak of $|\partial_z\tau_w|_{\max}$ and $|\partial_z p_w|_{\max}$ for the COPD and CF mucus cases observed in Figs. 9 and 11, their pressure and velocity fields are plotted in Fig. 13. The pressure contours are plotted on the right-hand side of each panel, and the velocity vectors are plotted on the left-hand side. Also, the top and bottom rows represent the healthy and CF mucus cases, respectively.

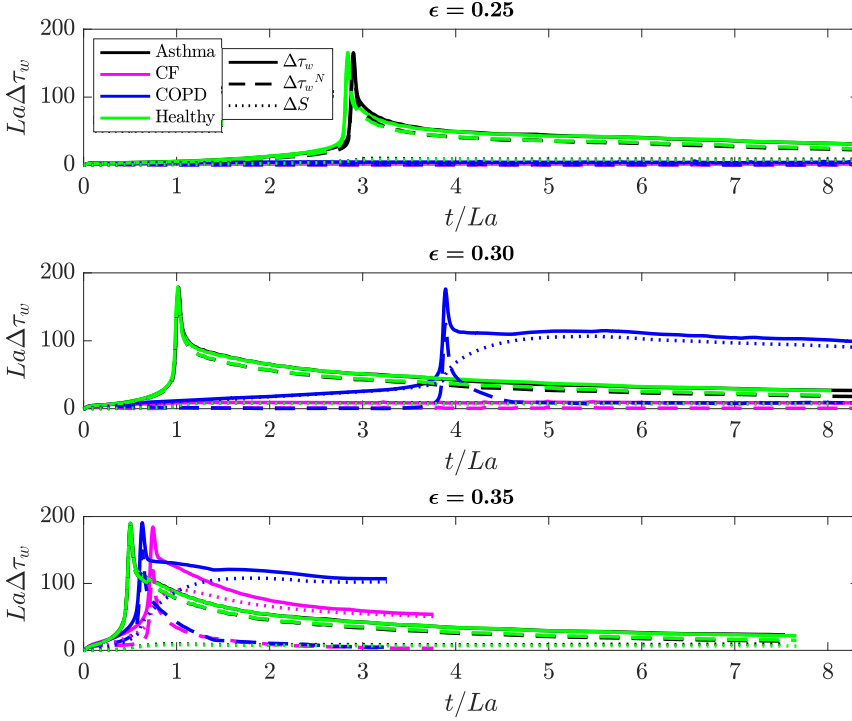


FIG. 12. Evolution of wall tangential stress excursion, $\Delta\tau_w = \max(\tau_w) - \min(\tau_w)$, which consists of Newtonian ($\Delta\tau^N$) and extrastress (ΔS) components, for $La = 300$ and $\epsilon = 0.25$ (top), $\epsilon = 0.30$ (middle), and $\epsilon = 0.35$ (bottom) for asthma (black lines), CF (magenta lines), COPD (blue lines), healthy (green lines), and Newtonian (cyan lines) cases. The wall tangential stress excursion $\Delta\tau_w$ and its Newtonian $\Delta\tau^N$ and extrastress ΔS components are represented by solid, dashed, and dotted lines, respectively. Note that the nondimensional time, t , is divided by La to eliminate the effect of surface tension, σ^* , on the timescaling for a better interpretation of the results. Stress excursion values are also rescaled by La for the same purpose.

Romanò *et al.* [43] stated that the peak of the local normal stress gradient is related to the capillary wave formed after the plug formation. When the air-liquid interface is compared between the healthy and the CF cases, it can be seen that the curvature formed by the healthy case is larger than that of the CF case (especially top-right and bottom-right snapshots). The larger elastic modulus of CF mucus makes the liquid layer stiffer, so its interface has a lower curvature compared to that of the healthy one. This can also be confirmed by the higher pressure gradient around the shoulder of the healthy mucus compared to the CF case.

This analysis is quantified in Fig. 14 by plotting the time evolution of the minimum and maximum core radius of air-liquid interface (R_{\min} and R_{\max}), and the mucus layer volume between the nondimensional axial locations of $z = 1.3$ and $z = 4.7$ (V) for the healthy, asthma, COPD, CF, and Newtonian cases. It should be noted that where R_{\max} is the highest, the liquid layer thickness is the smallest. The figure clearly shows that the maximum value of R_{\max} is smaller for the COPD and CF mucus cases, so this confirms that the air-liquid interface does not bend easily, and forms a capillary wave with a smaller curvature in these cases. Hence, the result is lower local normal and tangential stress peaks. This is also in agreement with the asymptotic theory for a Bretherton bubble [80] as Romanò *et al.* [81] pointed out, i.e., $\partial_z p_w \approx -\epsilon \partial_z^3 (1 - R_I)$.

Another important point is that the higher G of the COPD and CF mucus cases slow down the liquid accumulation at the center, thus making the whole process slower. This slower rate of liquid transfer to the liquid bulge results in lower velocity gradient around the wall, and consequently,

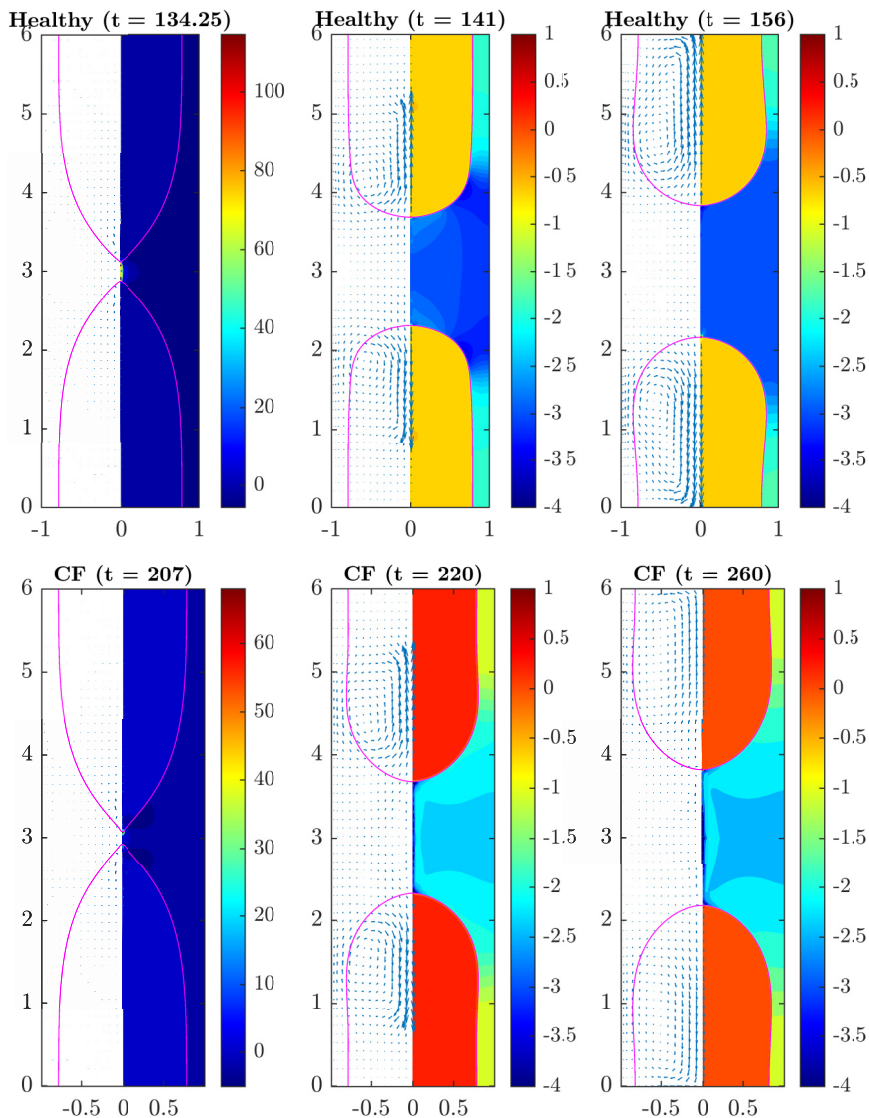


FIG. 13. Evolution of the interfaces (solid magenta lines) with constant contours of the pressure field (right portion of each subplot) and the velocity vectors (left portion of each subplot) for the healthy and the CF mucus ($La = 300$ and $\epsilon = 0.35$).

lower local shear stress gradients. A similar smearing effect has also been related to the increase of viscosity of the liquid layer before [43,47].

V. SUMMARY AND CONCLUSIONS

The effects of the non-Newtonian characteristics of the mucus on airway closure have been studied in a model problem, where an EVP liquid layer coats inside of a rigid pipe and surrounds the air core. The rheological properties of the EVP liquid layer have been determined by fitting the Saramito-HB model to the experimental data for the healthy, asthma, COPD, and CF mucus cases

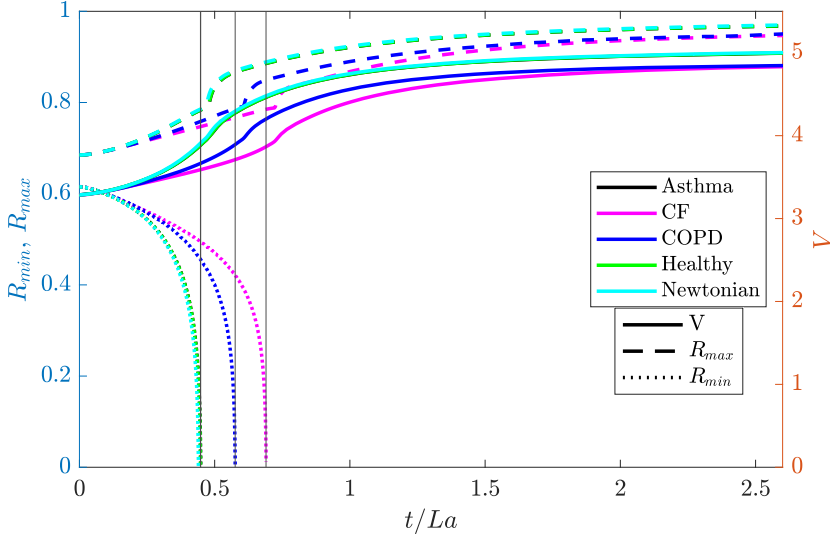


FIG. 14. Time evolution of the minimum and maximum core radius of air-liquid interface (R_{min} and R_{max}), and the mucus layer volume between the nondimensional axial locations of $z = 1.3$ and $z = 4.7$ (V) for healthy, asthma, COPD, CF, and Newtonian cases. The closure times are denoted by a black vertical solid line for each case. Note that the nondimensional time, t , is divided by La to eliminate the effect of surface tension, σ^* , on the timescaling for a better interpretation of the results ($La = 300$ and $\epsilon = 0.35$).

[19]. These mucus conditions are studied in varying Laplace number and initial mucus thickness conditions, and the possible effects on the wall stresses are analyzed.

First, the EVP parameters for four different conditions of airway mucus have been obtained by rheological fitting process similar to Fragedakis *et al.* [25]. Here the viscoelastic moduli G' and G'' are fitted to the experimental data by Patarin *et al.* [19], and the EVP model parameters G^* , n , K^* , and τ_y^* are determined for the healthy, asthma, COPD and CF cases. These parameters are used to examine the effects of the pathological conditions.

Yielded zones of asthma, COPD, and CF mucus are compared against the healthy one in both pre- and postcoalescence phases. In this comparison, it is found that the slightly higher τ_y^* of the asthma mucus causes less yielding during the closure. However, the profile of the yielded zones are very similar in both cases, and concentrated at the bulge tip and at the wall near the shoulder, where the tangential stresses are larger. On the other hand, the COPD mucus is an order of magnitude larger τ_y^* and G^* than those of the healthy mucus. The larger G^* results in a significant delay of the closure, while the larger τ_y^* increases the quantity of unyielded mucus, and results in a more solidlike behavior. Last, the comparison is made between the healthy and the CF conditions. Here it is shown that the CF mucus has considerably larger yielded regions than that of the healthy one. This counterintuitive behavior is attributed to the much larger elastic modulus of the CF mucus compared to the COPD mucus, which alters the Weissenberg number of both layers significantly. A similar behavior is reported by Izbassarov and Tammsola [79] for an EVP droplet in a Newtonian medium. In all cases, the EVP liquid layer is predominantly in unyielded state before the breakup suggesting that the elastic behavior and solvent viscosity are the main factors affecting the bulk fluid behavior before the closure.

Afterwards, the effect of the pathological conditions on the wall stresses are analyzed by varying surface tension (Laplace number) and initial mucus thickness conditions as recent findings suggest that these can be observed in pathological conditions of the airway [82–84]. This shows that the large G (small Wi) of the COPD and CF mucus inhibits the plug formation at low La values. It confirms that the elastic behavior of the fluid is dominant before the breakup and mainly affects whether the

closure occurs. The closure time, t_c , is also largely determined by G . The initial undisturbed liquid layer thickness, ϵ , was also varied at each studied La value to find out how the wall stresses and t_c are affected by this parameter, and it is found that as ϵ increases t_c converges to the Newtonian case in each pathological case.

The influence of the pathological cases on the wall stresses are also studied as these are important to estimate how the airway epithelium may be affected in these conditions. It is seen that the contribution from the viscoelastic stress (ΔS) on the total stress ($\Delta\tau$) at the peak stress levels is higher in the COPD and CF cases. Furthermore, ΔS relaxes very slowly after the closure, and stays almost as high as the Newtonian peak for a very long time. This continuous disturbance after the closure may increase the damage on the pulmonary epithelial cells.

Another important finding is that the high nondimensional stiffness (G) of the COPD and CF mucus causes smaller curvature at the capillary wave, and consequently smaller peaks of local normal stress gradients during the closure. The local tangential stress gradients are also smaller for the COPD and CF conditions because of the slower accumulation of liquid at the axial center of the domain. This indicates that the main source of stress for the pulmonary epithelium may be coming from the tangential and normal stress excursions in the COPD and CF mucus ($\Delta\tau_w$ and Δp_w).

These remarks suggest that the EVP model used in this paper can capture additional physics that have not been reported before. The increased peak of the stresses due to the extra stress contribution and the persisting extra stress after the closure may be especially important from the medical point of view, since they induce significant stress levels for the airway epithelium. As it is already known that CF and COPD can alter the mucus and surfactant secretion routines in the lungs [83,84], it is likely to observe airway closure in these patients. To decrease the damaging effects discussed above, therapeutic approaches such as inhaled hypertonic saline that aim to decrease the elasticity of airway mucus can be applied [85]. Moreover, further research can discuss liquid plug propagation and rupture in these conditions to analyze whether liquid plug formation damages the pulmonary epithelium repeatedly.

ACKNOWLEDGMENTS

Support from the Scientific and Technical Research Council of Turkey (TUBITAK), Grant No. 119M513, and National Institutes of Health (NIH), Grant No. HL136141, is kindly acknowledged.

-
- [1] E. R. Weibel and D. M. Gomez, Architecture of the human lung, *Science* **137**, 577 (1962).
 - [2] J. B. Grotberg, Respiratory fluid mechanics, *Phys. Fluids* **23**, 021301 (2011).
 - [3] J. B. West, *Respiratory Physiology: The Essentials* (Lippincott Williams & Wilkins, Philadelphia, 2012)
 - [4] D. Halpern, H. Fujioka, S. Takayama, and J. B. Grotberg, Liquid and surfactant delivery into pulmonary airways, *Respir. Physiol. Neurobiol.* **163**, 222 (2008).
 - [5] P. A. Gauglitz and C. J. Radke, An extended evolution equation for liquid film breakup in cylindrical capillaries, *Chem. Eng. Sci.* **43**, 1457 (1988).
 - [6] D. Halpern and J. B. Grotberg, Fluid-elastic instabilities of liquid-lined flexible tubes, *J. Fluid Mech.* **244**, 615 (1992).
 - [7] D. Halpern and J. B. Grotberg, Surfactant effects on fluid-elastic instabilities of liquid-lined flexible tubes: A model of airway closure, *J. Biomech. Eng.* **115**, 271 (1993).
 - [8] D. Halpern and J. B. Grotberg, Nonlinear saturation of the Rayleigh instability due to oscillatory flow in a liquid-lined tube, *J. Fluid Mech.* **492**, 251 (2003).
 - [9] M. Heil, A. L. Hazel, and J. A. Smith, The mechanics of airway closure, *Respir. Physiol. Neurobiol.* **163**, 214 (2008).
 - [10] R. D. Kamm and R. C. Schroter, Is airway closure caused by a liquid film instability? *Respir. Physiol.* **75**, 141 (1989).

- [11] J. B. Grotberg, Respiratory fluid mechanics and transport processes, *Annu. Rev. Biomed. Eng.* **3**, 421 (2001).
- [12] S. Girod, J. M. Zahm, C. Plotkowski, G. Beck, and E. Puchelle, Role of the physicochemical properties of mucus in the protection of the respiratory epithelium, *Eur. Respir. J.* **5**, 477 (1992).
- [13] S. K. Lai, Y. Y. Wang, D. Wirtz, and J. Hanes, Micro- and macrorheology of mucus, *Adv. Drug Deliv. Rev.* **61**, 86 (2009).
- [14] R. A. Cone, Barrier properties of mucus, *Adv. Drug Deliv. Rev.* **61**, 75 (2009).
- [15] S. E. Spagnolie, Complex fluids in biological systems, *Biol. Med. Phys. Biomed. Eng.* (2015).
- [16] D. B. Hill, P. A. Vasquez, J. Mellnik, S. A. McKinley, A. Vose, F. Mu, A. G. Henderson, S. H. Donaldson, N. E. Alexis, R. C. Boucher, and M. G. Forest, A biophysical basis for mucus solids concentration as a candidate biomarker for airways disease, *PLoS ONE* **9**, e87681 (2014).
- [17] O. Lafforgue, I. Seyssiecq, S. Poncet, and J. Favier, Rheological properties of synthetic mucus for airway clearance, *J. Biomed. Mater. Res. Part A* **106**, 386 (2018).
- [18] O. W. Williams, A. Sharafkhaneh, V. Kim, B. F. Dickey, and C. M. Evans, Airway mucus: From production to secretion, *Am. J. Respir. Cell Mol. Biol.* **34**, 527 (2006).
- [19] J. Patarin, É. Ghiringhelli, G. Darsy, M. Obamba, P. Bochu, B. Camara, S. Quétant, J.-L. Cracowski, C. Cracowski, and M. R. de Saint Vincent, Rheological analysis of sputum from patients with chronic bronchial diseases, *Sci. Rep.* **10**, 15685 (2020).
- [20] B. S. Schuster, J. S. Suk, G. F. Woodworth, and J. Hanes, Nanoparticle diffusion in respiratory mucus from humans without lung disease, *Biomaterials* **34**, 3439 (2013).
- [21] M. Dawson, D. Wirtz, and J. Hanes, Enhanced viscoelasticity of human cystic fibrotic sputum correlates with increasing microheterogeneity in particle transport, *J. Biol. Chem.* **278**, 50393 (2003).
- [22] C. Nettle, L. Jenkins, D. Curtis, N. Badiei, K. Lewis, P. Williams, and D. Daniels, Linear rheology as a potential monitoring tool for sputum in patients with chronic obstructive pulmonary disease (copd), *Biorheology* **54**, 67 (2018).
- [23] H. Nielsen, S. Hvidt, C. A. Sheils, and P. A. Janmey, Elastic contributions dominate the viscoelastic properties of sputum from cystic fibrosis patients, *Biophys. Chem.* **112**, 193 (2004).
- [24] P. Saramito, A new constitutive equation for elastoviscoplastic fluid flows, *J. Non-Newt. Fluid Mech.* **145**, 1 (2007).
- [25] D. Fraggedakis, Y. Dimakopoulos, and J. Tsamopoulos, Yielding the yield stress analysis: A thorough comparison of recently proposed elasto-visco-plastic (EVP) fluid models, *J. Non-Newt. Fluid Mech.* **236**, 104 (2016).
- [26] B. Gueslin, L. Talini, B. Herzhaft, Y. Peysson, and C. Allain, Flow induced by a sphere settling in an aging yield-stress fluid, *Phys. Fluids* **18**, 103101 (2006).
- [27] A. Putz, T. Burgehelea, I. Frigaard, and D. Martinez, Settling of an isolated spherical particle in a yield stress shear thinning fluid, *Phys. Fluids* **20**, 033102 (2008).
- [28] Y. Holenberg, O. M. Lavrenteva, A. Liberzon, U. Shavit, and A. Nir, PTV and PIV study of the motion of viscous drops in yield stress material, *J. Non-Newt. Fluid Mech.* **193**, 129 (2013).
- [29] A. Beris, J. Tsamopoulos, R. Armstrong, and R. Brown, Creeping motion of a sphere through a bingham plastic, *J. Fluid Mech.* **158**, 219 (1985).
- [30] P. R. de Souza Mendes, Dimensionless non-newtonian fluid mechanics, *J. Non-Newt. Fluid Mech.* **147**, 109 (2007).
- [31] S. Bénito, C. H. Bruneau, T. Colin, C. Gay, and F. Molino, An elasto-visco-plastic model for immortal foams or emulsions, *Eur. Phys. J. E* **25**, 225 (2008).
- [32] Y. S. Park and P. L. Liu, Oscillatory pipe flows of a yield-stress fluid, *J. Fluid Mech.* **658**, 211 (2010).
- [33] F. Belblidia, H. R. Tamaddon-Jahromi, M. F. Webster, and K. Walters, Computations with viscoplastic and viscoelastoplastic fluids, *Rheol. Acta* **50**, 343 (2011).
- [34] T. C. Papanastasiou, Flows of materials with yield, *J. Rheol.* **31**, 385 (1987).
- [35] J. G. Oldroyd, On the formulation of rheological equations of state, *Proc. R. Soc. Lond. A* **200**, 523 (1950).
- [36] P. Saramito, A new elastoviscoplastic model based on the Herschel-Bulkley viscoplastic model, *J. Non-Newt. Fluid Mech.* **158**, 154 (2009).

- [37] A. M. Bilek, K. C. Dee, and D. P. Gaver, Mechanisms of surface-tension-induced epithelial cell damage in a model of pulmonary airway reopening, *J. Appl. Physiol.* **94**, 770 (2003).
- [38] S. S. Kay, A. M. Bilek, K. C. Dee, and D. P. Gaver, Pressure gradient, not exposure duration, determines the extent of epithelial cell damage in a model of pulmonary airway reopening, *J. Appl. Physiol.* **97**, 269 (2004).
- [39] D. Huh III, H. Fujioka, Y. C. Tung, N. Futai, R. Paine, J. B. Grotberg, and S. Takayama, Acoustically detectable cellular-level lung injury induced by fluid mechanical stresses in microfluidic airway systems, *Proc. Natl. Acad. Sci. USA* **104**, 18886 (2007).
- [40] H. Tavana, P. Zamankhan, P. J. Christensen, J. B. Grotberg, and S. Takayama, Epithelium damage and protection during reopening of occluded airways in a physiologic microfluidic pulmonary airway model, *Biomed Microdev.* **13**, 731 (2011).
- [41] S. Bian, C. F. Tai, D. Halpern, Y. Zheng, and J. B. Grotberg, Experimental study of flow fields in an airway closure model, *J. Fluid Mech.* **647**, 391 (2010).
- [42] C. F. Tai, S. Bian, D. Halpern, Y. Zheng, M. Filoche, and J. B. Grotberg, Numerical study of flow fields in an airway closure model, *J. Fluid Mech.* **677**, 483 (2011).
- [43] F. Romanò, H. Fujioka, M. Muradoglu, and J. B. Grotberg, Liquid plug formation in an airway closure model, *Phys. Rev. Fluids* **4**, 093103 (2019).
- [44] D. Halpern, H. Fujioka, and J. B. Grotberg, The effect of viscoelasticity on the stability of a pulmonary airway liquid layer, *Phys. Fluids* **22**, 011901 (2010).
- [45] F. Romanò, M. Muradoglu, H. Fujioka, and J. B. Grotberg, The effect of viscoelasticity in an airway closure model, *J. Fluid Mech.* **913**, A31 (2021).
- [46] J. D. Shemilt, A. Horsley, O. E. Jensen, A. B. Thompson, and C. A. Whitfield, Surface-tension-driven evolution of a viscoplastic liquid coating the interior of a cylindrical tube, *J. Fluid Mech.* **944**, A22 (2022).
- [47] O. Erken, F. Romanò, J. Grotberg, and M. Muradoglu, Capillary instability of a two-layer annular film: An airway closure model, *J. Fluid Mech.* **934**, A7 (2022).
- [48] P. Zamankhan, B. T. Helenbrook, S. Takayama, and J. B. Grotberg, Steady motion of bingham liquid plugs in two-dimensional channels, *J. Fluid Mech.* **705**, 258 (2012).
- [49] Y. Hu, S. Bian, J. Grotberg, M. Filoche, J. White, S. Takayama, and J. B. Grotberg, A microfluidic model to study fluid dynamics of mucus plug rupture in small lung airways, *Biomicrofluidics* **9**, 044119 (2015).
- [50] Y. Hu, F. Romanò, and J. B. Grotberg, Effects of surface tension and yield stress on mucus plug rupture: A numerical study, *J. Biomech. Eng.* **142**, 061007 (2020).
- [51] P. Zamankhan, S. Takayama, and J. B. Grotberg, Steady displacement of long gas bubbles in channels and tubes filled by a bingham fluid, *Phys. Rev. Fluids* **3**, 013302 (2018).
- [52] S. A. Bahrani, S. Hamidouche, M. Moazzen, K. Seck, C. Duc, M. Muradoglu, J. B. Grotberg, and F. Romanò, Propagation and rupture of elastoviscoplastic liquid plugs in airway reopening model, *J. Non-Newt. Fluid Mech.* **300**, 104718 (2022).
- [53] D. Fraggedakis, Y. Dimakopoulos, and J. Tsamopoulos, Yielding the yield-stress analysis: A study focused on the effects of elasticity on the settling of a single spherical particle in simple yield-stress fluids, *Soft Matter* **12**, 5378 (2016).
- [54] S. O. Unverdi and G. Tryggvason, A front-tracking method for viscous, incompressible, multi-fluid flows, *J. Comput. Phys.* **100**, 25 (1992).
- [55] D. Izbassarov and M. Muradoglu, A front-tracking method for computational modeling of viscoelastic two-phase flow systems, *J. Non-Newt. Fluid Mech.* **223**, 122 (2015).
- [56] D. Izbassarov, M. E. Rosti, M. N. Ardekani, M. Sarabian, S. Hormozi, L. Brandt, and O. Tammisola, Computational modeling of multiphase viscoelastic and elastoviscoplastic flows, *Int. J. Numer. Methods Fluids* **88**, 521 (2018).
- [57] C. S. Peskin, Numerical analysis of blood flow in the heart, *J. Comput. Phys.* **25**, 220 (1977).
- [58] A. J. Chorin, Numerical solution of the Navier-Stokes equations, *Math. Comp.* **22**, 745 (1968).
- [59] G. Tryggvason, B. Bunner, A. Esmaeeli, D. Juric, N. Al-Rawahi, W. Tauber, J. Han, S. Nas, and Y. J. Jan, A front-tracking method for the computations of multiphase flow, *J. Comput. Phys.* **169**, 708 (2001).
- [60] M. Muradoglu, F. Romanò, H. Fujioka, and J. B. Grotberg, Effects of surfactant on propagation and rupture of a liquid plug in a tube, *J. Fluid Mech.* **872**, 407 (2019).

- [61] U. Olgac, A. D. Kayaalp, and M. Muradoglu, Buoyancy-driven motion and breakup of viscous drops in constricted capillaries, *Int. J. Multiphase Flow* **32**, 1055 (2006).
- [62] G. Tryggvason, R. Scardovelli, and S. Zaleski, *Direct Numerical Simulations of Gas–Liquid Multiphase Flows* (Cambridge University Press, Cambridge, UK, 2011).
- [63] S. Popinet, Basilisk, <http://basilisk.fr>.
- [64] E. Chaparian and O. Tammisola, An adaptive finite element method for elastoviscoplastic fluid flows, *J. Non-Newtonian Fluid Mech.* **271**, 104148 (2019).
- [65] E. Breatnach, G. C. Abbott, and R. G. Fraser, Dimensions of the normal human trachea, *Am. J. Roentgenol.* **142**, 903 (1984).
- [66] E. J. Burger and P. Macklem, Airway closure: Demonstration by breathing 100 percent O₂ at low lung volumes and by N₂ washout., *J. Appl. Physiol.* **25**, 139 (1968).
- [67] R. G. Crystal, *The Lung: Scientific Foundations* (Lippincott, Philadelphia, PA, 1997).
- [68] H. Kitaoka, R. Takaki, and B. Suki, A three-dimensional model of the human airway tree, *J. Appl. Physiol.* **87**, 2207 (1999).
- [69] J. Moriarty and J. Grotberg, Flow-induced instabilities of a mucus-serous bilayer, *J. Fluid Mech.* **397**, 1 (1999).
- [70] S. Schürch, P. Gehr, V. Im Hof, M. Geiser, and F. Green, Surfactant displaces particles toward the epithelium in airways and alveoli, *Respir. Physiol.* **80**, 17 (1990).
- [71] J. Zahm, M. King, C. Duvivier, D. Pierrot, S. Girod, and E. Puchelle, Role of simulated repetitive coughing in mucus clearance, *Eur. Respir. J.* **4**, 311 (1991).
- [72] C. J. Dimitriou, R. H. Ewoldt, and G. H. McKinley, Describing and prescribing the constitutive response of yield stress fluids using large amplitude oscillatory shear stress (laostress), *J. Rheol.* **57**, 27 (2013).
- [73] K. Hyun, M. Wilhelm, C. O. Klein, K. S. Cho, J. G. Nam, K. H. Ahn, S. J. Lee, R. H. Ewoldt, and G. H. McKinley, A review of nonlinear oscillatory shear tests: Analysis and application of large amplitude oscillatory shear (laos), *Prog. Polym. Sci.* **36**, 1697 (2011).
- [74] M.-C. Yang, L. Scriven, and C. Macosko, Some rheological measurements on magnetic iron oxide suspensions in silicone oil, *J. Rheol.* **30**, 1015 (1986).
- [75] MATLAB, *9.9.0.1592791 (R2020b) Update 5* (The MathWorks Inc., Natick, MA, 2020).
- [76] K. Joyner and G. A. Duncan, Reliably sourced airway mucus, *Am. J. Physiol.-Lung Cell. Molec. Physiol.* **317**, L496 (2019).
- [77] J. Y. Lock, T. L. Carlson, and R. L. Carrier, Mucus models to evaluate the diffusion of drugs and particles, *Adv. Drug Deliv. Rev.* **124**, 34 (2018).
- [78] E. Chaparian, D. Izbassarov, F. De Vita, L. Brandt, and O. Tammisola, Yield-stress fluids in porous media: A comparison of viscoplastic and elastoviscoplastic flows, *Meccanica* **55**, 331 (2020).
- [79] D. Izbassarov and O. Tammisola, Dynamics of an elastoviscoplastic droplet in a newtonian medium under shear flow, *Phys. Rev. Fluids* **5**, 113301 (2020).
- [80] F. P. Bretherton, The motion of long bubbles in tubes, *J. Fluid Mech.* **10**, 166 (1961).
- [81] F. Romanò, M. Muradoglu, and J. B. Grotberg, Effect of surfactant in an airway closure model, *Phys. Rev. Fluids*, **7**, 093103 (2022).
- [82] V. De Rose, K. Molloy, S. Gohy, C. Pilette, and C. M. Greene, Airway epithelium dysfunction in cystic fibrosis and COPD, *Mediat. Inflamm.* **2018** (2018).
- [83] C. W. Agudelo, B. K. Kumley, E. Area-Gomez, Y. Xu, A. J. Dabo, P. Geraghty, M. Campos, R. Foronjy, and I. Garcia-Arcos, Decreased surfactant lipids correlate with lung function in chronic obstructive pulmonary disease (copd), *PLoS One* **15**, e0228279 (2020).
- [84] M. Griese, P. Birrer, and A. Demirsoy, Pulmonary surfactant in cystic fibrosis, *Eur. Respir. J.* **10**, 1983 (1997).
- [85] J. V. Fahy and B. F. Dickey, Airway mucus function and dysfunction, *N. Engl. J. Med.* **363**, 2233 (2010).